



**High Resolution 3D Winds Derived from a Newly Developed WISSDOM
Synthesis Scheme using Multiple Doppler Lidars and Observations**

Chia-Lun Tsai¹, Kwonil Kim¹, Yu-Chieng Liou², and Gyuwon Lee^{*1}

¹Department of Astronomy and Atmospheric Sciences, Center for Atmospheric REmote
sensing (CARE), Kyungpook National University, Daegu, South Korea

²Department of Atmospheric Sciences, National Central University, Jhongli, Taiwan

* Corresponding author: Prof. Gyuwon Lee, E-mail: gyuwon@knu.ac.kr



27 Abstract

28 A WISSDOM (Wind Synthesis System using Doppler Measurements) synthesis scheme was
29 developed to derive high-resolution 3-dimensional (3D) winds under clear-air conditions. From
30 this variational-based scheme, detailed wind information was obtained from scanning Doppler
31 lidars, automatic weather stations (AWSs), sounding observations, and local reanalysis datasets
32 (LDAPS, Local Data Assimilation and Prediction System), which were utilized as constraints to
33 minimize the cost function. The objective of this study is to evaluate the performance and
34 accuracy of derived 3D winds from this newly developed scheme. A strong wind event was
35 selected to demonstrate its performance over complex terrain in Pyeongchang, South Korea. The
36 size of the test domain is $12 \times 12 \text{ km}^2$ extended up to 3 km height mean sea level (MSL) with
37 remarkably high horizontal and vertical resolution of 50 m. The derived winds reveal that
38 reasonable patterns were explored from a control run, as they have high similarity with the
39 sounding observations. The results of intercomparisons show that the correlation coefficients
40 between derived horizontal winds and sounding observations are 0.97 and 0.87 for u- and v-
41 component winds, respectively, and the averaged bias (root mean square deviation, RMSD) of
42 horizontal winds is between -0.78 and 0.09 (1.72 and 1.65) m s^{-1} . The correlation coefficients
43 between WISSDOM-derived winds and lidar QVP (quasi-vertical profile) are 0.84 and 0.35 for
44 u- and v-component winds, respectively, and the averaged bias (RMSD) of horizontal winds is
45 between 2.83 and 2.26 (3.69 and 2.92) m s^{-1} . The statistical errors also reveal a satisfying
46 performance of the retrieved 3D winds; the median values of wind directions are $-5 \sim 5$ ($0 \sim 2.5$)
47 degrees, the wind speed is approximately $-1 \sim 3 \text{ m s}^{-1}$ ($-1 \sim 0.5 \text{ m s}^{-1}$) and the vertical velocity is
48 $-0.2 \sim 0.6 \text{ m s}^{-1}$ compared with the lidar QVP (sounding observations). A series of sensitivity tests
49 with different weighting coefficients, radius of influence (RI) in interpolation and various
50 combination of different datasets were also performed, and the results indicate that the present
51 setting of the control run is the best reference to WISSDOM synthesis in this event.

52



53 1. Introduction

54 In the past few decades, many practical methods have been developed to derive wind
55 information by using meteorological radar data (Mohr and Miller, 1983, Lee et al., 1994, Liou
56 and Chang, 2009, Bell et al. 2012). The derived winds substantially revealed reasonable patterns
57 compared with conventional observations (such as surface stations, soundings, wind profiles,
58 etc.) and models (Liou et al., 2014, North et al., 2017, Chen, 2019, Oue et al., 2019). Most
59 comprehensive applications of the derived winds were adopted to document kinematic and
60 precipitation structures associated with various weather systems at different scales (Yu and Tsai,
61 2013, Yu and Tsai, 2017, Tsai et al. 2018, Yu et al., 2020, Cha and Bell, 2021, Tsai et al., 2022).
62 In addition, the accuracy of 3D winds could be improved when increasing the numbers of Doppler
63 radar because relatively fewer assumptions and more information can be included (Yu and Tsai
64 2010, Liou and Chang, 2009). Therefore, the retrieved schemes within multiple Doppler radars
65 are a more popular way to obtain high-quality 3D winds and have been extensively applied to
66 meteorological analyses.

67 The technique of velocity track display (VTD, Lee et al., 1994) and ground-based velocity
68 track display (GBVTD, Lee et al., 1999) can derive the winds from single Doppler radar under
69 some assumptions, as the wind patterns are generally uniform or axisymmetric rotational (Cha
70 and Bell, 2021). More extended techniques based on VTD and GBVTD have also been applied
71 to increase the quality of derived wind data, and such techniques include EGBVTD (Liou et al.,
72 2006) and generalized velocity track display (GVTD, Jou et al., 2008). However, winds usually
73 present nonuniform patterns and fast-evolving characteristics in most mesoscale weather systems
74 and microscale phenomena, and complete and detailed winds are still difficult to resolve by these
75 techniques. Instead of a single Doppler radar, multiple Doppler can retrieve better quality 3D
76 winds with relatively fewer assumptions because they provide sufficient radial velocity
77 measurements and wind information with wider coverage in the synthesis domain.

78 CEDRIC (Cartesian Space Editing, Synthesis, and Display of Radar Fields under Interactive



Control, Mohr and Miller, 1983) is a traditional package used to retrieve 3D winds by dual-Doppler radar observations. This scheme usually determines the horizontal winds by using two radars, and the vertical velocity can be obtained by variational adjustment with anelastic continuity equation. Spline Analysis at Mesoscale Utilizing Radar and Aircraft Instrumentation (SAMURAI) software is another way to retrieve 3D winds (Bell et al., 2012); this scheme is a kind of variational data assimilation that adopts multiple radars. These two schemes were mainly developed by NCAR (National Center Atmospheric Research) and Colorado State University, and they are both open resources available on the websites of LROSE (Lidar Radar Open Software Environment, <http://lrose.net> and <https://github.com/NCAR/lrose-cedric>). Recently, Tsai et al. (2018) utilized the measurements of six Doppler radars to document precipitation and airflow structures over complex terrain on the northeastern coast of South Korea via WISSDOM (Wind Synthesis System using Doppler Measurements, Liou and Chang, 2009, Liou et al., 2012, Liou et al., 2016) synthesis. Since one of the advantages of WISSDOM is that it considers the orographic forcing on Cartesian coordinates by applying IBM (immersed boundary method, Tseng and Ferziger, 2003), higher quality 3D winds can be derived well over terrain (Liou et al., 2013, 2014, Lee et al., 2018).

Generally, radial velocity is measured by detecting the movement of precipitation particles relative to the locations of Doppler radars; thus, there are no sufficient radial velocity measurements under clear-air conditions. However, the winds in clear-air conditions usually play an important role in the initiations of various weather systems and phenomena, such as downslope winds, gap winds, and wildfires (Reed, 1931, Colle and Mass, 2000, Mass and Ovens, 2019, Lee et al., 2020). Although surface stations, soundings, and wind profilers can measure winds under clear-air conditions, relatively poor spatial coverage is still a problem for obtaining sufficient wind information in certain local areas. Therefore, scanning Doppler lidars will be one approach to obtain wind information under clear-air conditions. Päsche et al. (2015) assessed the quality of wind derived by Doppler lidar with a wind profiler in a year trial, and the results showed good



105 agreement in wind speed (the error ranged between 0.5 and 0.7 m s⁻¹) and wind direction (the
106 error ranged between 5° and 10°). Bell et al. (2020) used an intersecting range height indicator
107 (RHI) of six Doppler lidars to build “virtual towers” (such as wind profilers) to investigate the
108 airflow over complex terrain during the Perdigão experiment. These virtual towers can fill the
109 gap in wind measurements above conventional physical towers. The uncertainty of wind fields is
110 also reduced by adopting multiple Doppler lidars (Choukulkar et al., 2017), and a high
111 spatiotemporal resolution of derived wind is allowed to check small-scale rotors in mountainous
112 areas (Hill et al., 2010).

113 The original WISSDOM was designed to retrieve 3D winds based on Doppler radar
114 observations and background inputs combined with conventional observations and modeling.
115 However, the original WISSDOM only provided 3D winds under precipitation conditions and
116 not under clear-air conditions because the radar usually cannot detect radial velocity without
117 precipitation particles. To obtain high-quality 3D winds under clear-air conditions, the radial
118 velocity observed from the scanning Doppler lidars can be used in WISSDOM. Furthermore, the
119 conventional observations and modeling datasets were used as isolated constraints in the
120 modified WISSDOM synthesis scheme. One of the benefits of the isolated constraints is that it is
121 easy to synthesize any kind of wind information obtained from available datasets and give
122 suitable weighting coefficients with different constraints when they are processing the
123 minimization in the cost function. Thus, more reliable 3D winds in clear-air conditions were well
124 derived from this newly developed WISSDOM synthesis scheme.

125 The objective of this study is to modify the WISSDOM synthesis scheme based on the
126 original version to be a more flexible and useful scheme by adding any number of Doppler lidars
127 and conventional observations as well as modeling datasets. This newly developed WISSDOM
128 will allow us to obtain an exceedingly high spatial resolution of 3D winds (50 m was set in this
129 study) under clear- air conditions. A variety of adequate datasets were collected during a strong
130 wind event in the winter season during an intensive field experiment ICE-POP 2018



(International Collaborative Experiments for Pyeongchang 2018 Olympic and Paralympic winter games). In this study, detailed principles of the newly developed WISSDOM and data implementation are elucidated in the following sections. In addition, the newly developed WISSDOM was performed to retrieve 3D winds over complex terrain under clear-air conditions in a strong wind event. The reliability of the derived 3D winds was also evaluated with conventional observations.

2. Methodology

2.1 Original version of WISSDOM (WInd Synthesis System using DOppler Measurements)

WISSDOM is a mathematically variational-based scheme to minimize the cost function, and various wind-related observations can be used as one of the constraints in the cost function. The 3D winds were derived by variationally adjusted solutions to satisfy the constraints in the cost function. The original version of WISSDOM performed five constraints, including radar observations (i.e., reflectivity and radial velocity), background (combined with automatic weather stations, sounding, model or reanalysis data), continuity equation, vorticity equation, and Laplacian smoothing (Liou and Chang, 2009, Liou et al., 2012, Liou et al. 2016, Tsai et al., 2018). The cost function can be expressed as

$$J = \sum_{M=1}^5 J_M, \quad (1)$$

where J_M is the different constraints. J_1 is the constraint related to the geometric relation between radar radial Doppler velocity observations (V_r) and derived one from true winds ($\mathbf{V}_t = u_t \mathbf{i} + v_t \mathbf{j} + w_t \mathbf{k}$) in Cartesian coordinates [eq. (2)].

$$J_1 = \sum_{t=1}^2 \sum_{x,y,z} \sum_{i=1}^N \alpha_{1,i} (T_{1,i,t})^2. \quad (2)$$



152 Since WISSDOM is a scheme that uses the 4DVAR approach, the variations between different
 153 time steps (t) should be considered, and two time (t) steps of radar observations were collected
 154 in this constraint. The x, y, z indicates the locations of a given grid point in the synthesis domain,
 155 and i could be any number (N) of radars (at least 1). The α_1 is the weighting coefficient of
 156 J_1 (α_2 is the weighting coefficient of J_2 and so on). $T_{1,i,t}$ in eq. (2) is defined as eq. (3):

$$157 \quad T_{1,i,t} = (V_r)_{i,t} - \frac{(x - P_x^i)}{r_i} u_t - \frac{(y - P_y^i)}{r_i} v_t - \frac{(z - P_z^i)}{r_i} (w_t - W_{T,t}), \quad (3)$$

158 $(V_r)_{i,t}$ is the radial velocity observed by the radar (i) at time step (t), P_x^i, P_y^i and P_z^i depict the
 159 coordinate of radar i . The u_t, v_t and w_t ($W_{T,t}$) denote the 3D winds (terminal velocity of
 160 precipitation particles) at given grid points at the time step t ; and $r_i =$

$$161 \quad \sqrt{(x - P_x^i)^2 + (y - P_y^i)^2 + (z - P_z^i)^2}.$$

162 The second constraint is the difference between the background ($\mathbf{V}_{B,t}$) and true (derived)
 163 wind field ($\mathbf{V}_t = u_t \mathbf{i} + v_t \mathbf{j} + w_t \mathbf{k}$), which is defined as

$$164 \quad J_2 = \sum_{t=1}^2 \sum_{x,y,z} \alpha_2 (\mathbf{V}_t - \mathbf{V}_{B,t})^2. \quad (4)$$

165 There were several options to obtain background in the original version of WISSDOM. The most
 166 popular background resource involves using sounding observations; however, it can only provide
 167 homogeneous wind information for each level in WISSDOM with relatively coarse temporal
 168 resolution (3- to 12-hour intervals). The other option is combining sounding observations with
 169 AWS (automatic weather station) observations. Although the AWS provided wind information
 170 with better temporal resolution (1-min), the data were only observed at the surface layer with
 171 semirandom distributions. The last option is to combine sounding, AWS, modeling or reanalysis
 172 datasets. However, various datasets with different spatiotemporal resolutions are not favorable
 173 for appropriate interpolation of given grid points of WISSDOM synthesis, and the accuracy and
 174 reliability of the background may have been significantly affected by such a variety of datasets.
 175 Thus, these different observed or model data should be treated differently to minimize the



176 uncertainties and improve the accuracy. Thus, one of the improvements in the newly developed
 177 WISSDOM is that these inputs were separated into independent constraints individually. Note
 178 that the sounding observations are still a necessary dataset because the air density and temperature
 179 profile were used to identify the height of the melting level. In this study, sounding winds were
 180 adopted to represent the background for each level and a constraint at the same time; nevertheless,
 181 the AWS and reanalysis dataset are independent constraints in the newly developed WISSDOM
 182 (details are provided in the following section).

183 The third, fourth and fifth constraints in the cost function are the anelastic continuity
 184 equation, vertical vorticity equation and Laplacian smoothing filter, respectively. Equations (5),
 185 (6) and (7) are denoted as follows:

$$186 \quad J_3 = \sum_{t=1}^2 \sum_{x,y,z} \alpha_3 \left[\frac{\partial(\rho_0 u_t)}{\partial x} + \frac{\partial(\rho_0 v_t)}{\partial y} + \frac{\partial(\rho_0 w_t)}{\partial z} \right]^2, \quad (5)$$

$$187 \quad J_4 = \sum_{x,y,z} \alpha_4 \left\{ \frac{\partial \zeta}{\partial t} + \left[u \frac{\partial \zeta}{\partial x} + v \frac{\partial \zeta}{\partial y} + w \frac{\partial \zeta}{\partial z} + (\zeta + f) \left(\frac{\partial u}{\partial x} + \frac{\partial v}{\partial y} \right) + \left(\frac{\partial w}{\partial x} \frac{\partial v}{\partial y} - \frac{\partial w}{\partial y} \frac{\partial u}{\partial z} \right) \right] \right\}^2, \quad (6)$$

$$188 \quad J_5 = \sum_{t=1}^2 \sum_{x,y,z} \alpha_5 [\nabla^2(u_t + v_t + w_t)]^2. \quad (7)$$

189 ρ_0 in eq. (5) is the air density, and $\zeta = \partial v / \partial x - \partial u / \partial y$ in eq. (6).

190 2.2 The newly developed WISSDOM

191 In addition to the five constraints in the original version, the newly developed WISSDOM
 192 synthesis scheme includes three more constraints in the cost function. Thus, the cost function in
 193 the newly developed WISSDOM was written as

$$194 \quad J = \sum_{M=1}^8 J_M. \quad (8)$$

195 $J_1 \sim J_5$ in (8) are the same constraints corresponding to equations (2)-(7). The main purpose
 196 of this study is to retrieve 3D winds under clear-air conditions in which observational data are



197 relatively rare. Instead of the radial velocity $(V_r)_{i,t}$ observed from Doppler radars in eq. (3), the
 198 radial velocity observed from Doppler or wind lidars was adopted in the newly developed
 199 WISSDOM synthesis. In addition, if there were no precipitation particles under clear-air
 200 conditions, the terminal velocity of precipitation particles $(W_{T,t})$ was set to zero in eq. (3).

201 The sixth constraint is the difference between the derived wind fields and the sounding
 202 observations $(\mathbf{V}_{S,t})$, as defined in (9):

$$203 \quad J_6 = \sum_{t=1}^2 \sum_{x,y,z} \alpha_6 (V_t - V_{S,t})^2. \quad (9)$$

204 The sounding data in J_6 were interpolated to the given grid points near its tracks bearing on the
 205 radius influence (RI) distance (the details are provided in Section 3.2.3). The main difference
 206 between J_6 and J_2 is that the sounding data were used as an observation for given 3D locations,
 207 instead of the constraint of homogeneous background winds for each level in the studied domain.
 208 The seventh constraint represents the discrepancy between the true (derived) wind fields and
 209 AWS $(\mathbf{V}_{A,t})$, as expressed in (8):

$$210 \quad J_7 = \sum_{t=1}^2 \sum_{x,y,z} \alpha_7 (V_t - V_{A,t})^2. \quad (8)$$

211 Finally, the eighth constraint measures the misfit between the derived winds and the local
 212 reanalysis dataset $(\mathbf{V}_{L,t})$, as defined in (9):

$$213 \quad J_8 = \sum_{t=1}^2 \sum_{x,y,z} \alpha_8 (V_t - V_{L,t})^2. \quad (9)$$

214 In this study, various observations and reanalysis datasets were utilized as constraints in the cost
 215 function of WISSDOM. The most important dataset is the radial velocity observed from Doppler
 216 lidars, which can measure wind information with high spatial resolution and good coverage from
 217 near the surface up to higher layers in the test domain. Sounding and AWS can provide horizontal
 218 winds for background or to be included in the constraints. The local reanalysis datasets were
 219 obtained from the 3DVAR LDAPS (Local Data Assimilation and Prediction System) data



assimilation system from the KMA (Korea Meteorological Administration). Since these datasets have different coordinate systems and various spatiotemporal resolutions, additional procedures are required before the synthesis. Detailed descriptions of the procedures are described in the next section.

The high-quality synthesized 3D wind field from radar observations has been applied in several previous studies such as those by Liou and Chang (2009), Liou et al. (2012, 2013, 2014, 2016), and Lee et al. (2017). The advantages and details of the WISSDOM can be found in Tsai et al. (2018). This newly developed WISSDOM synthesis scheme has also been applied in the analysis related to the mechanisms of orographically induced strong wind on the northeastern coast of Korea (Tsai et al., 2022).

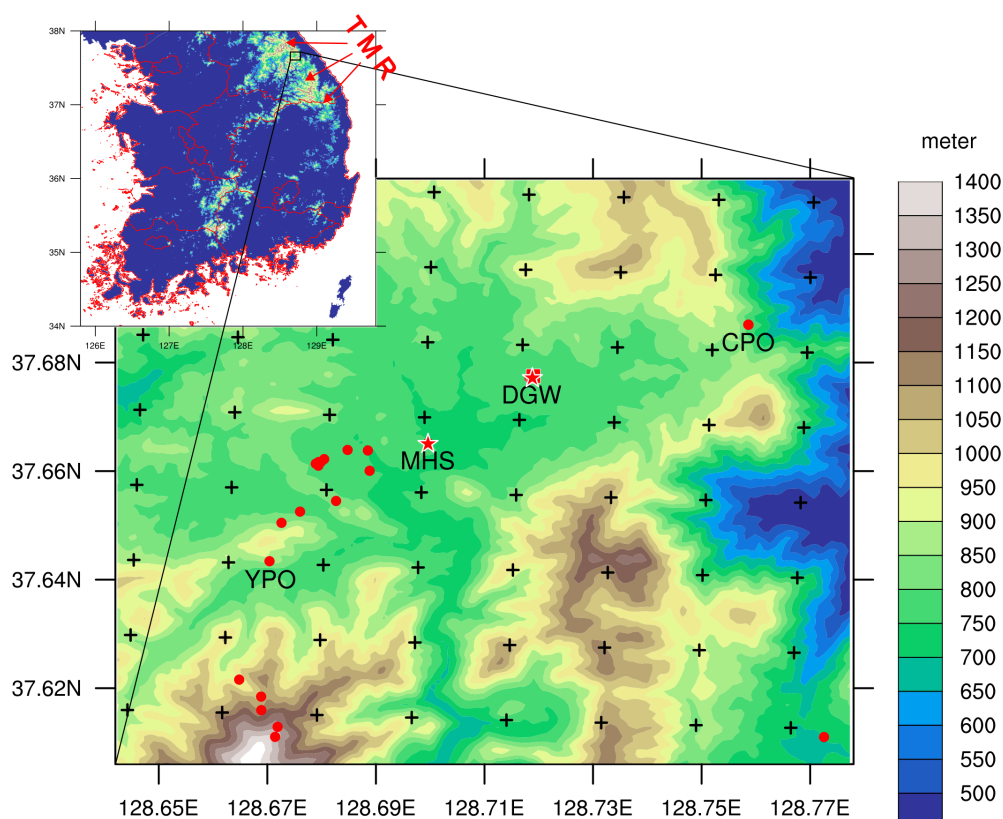
3. Data processing with a strong wind event

3.1 Basic information of WISSDOM synthesis

A small domain near the northeastern coast of South Korea was selected to derive detailed 3D winds over complex terrain (in the black box in the inset map in Fig. 1) because relatively dense and high-quality wind observations were only collected in this region during ICE-POP 2018. The size of the WISSDOM synthesis domain is $12 \times 12 \text{ km}^2$ (up to 3 km MSL height) in the horizontal (vertical) direction with 50 m grid spacing. Such high spatial resolution 3D winds were synthesized every 1 hour in this test. Note that the output time steps are adjustable to be finer, but they are highly related to the temporal resolution of various datasets and computing resources. Two scanning Doppler lidars are located near the center of the domain: one is the equipped “WINDEX-2000” (the model’s name from the manufacturer) at the MHS site, and the other is the “Stream line-XR” at the DGW site. In addition to the operational AWSs (727 stations), additional surface observations (32 stations) are also involved in ICE-POP 2018



243 surrounding the MHS and DGW sites and the venues of the winter Olympic Games. The
 244 soundings are launched at the DGW site every 3 hours during the research period. The LDAPS
 245 also provided high spatial resolution of wind information in the test domain. The horizontal
 246 distribution of all instruments and datasets used are shown in Fig. 1.



247 Figure 1. Horizontal distribution of instruments and datasets used in this study. A small box in the upper map
 248 indicates the WISSDOM synthesis domain. The Doppler lidars are marked by asterisks at the MHS and DGW
 249 sites. Red solid circles and squares indicate the automatic weather station (AWS) and sounding, respectively.
 250 The black cross marks the data points of LDAPS. Topographic features and elevations are shown with the color
 251 shading in a color bar in the figure. The location of the Teabek Mountain Range (TMR) is also marked.
 252

253 3.2 Data implemented in WISSDOM synthesis

254 3.2.1 Scanning Doppler lidars

255 The radial velocity observed from two scanning Doppler lidars was utilized to retrieve 3D



winds via WISSDOM synthesis. The original coordinate system of observed lidar data is not a Cartesian coordinate system, but spherical (or polar) coordinate system. In the lidar data collection, the lasers were emitted from the transmitter with rotating azimuth angles at an initial elevation angle, and the scanner increased the elevation angles when surveillance (likely between 0° and 360° clockwise from north) or PPI (plan position indicator) was finished. The data were collected by raising the elevation angles until the expected maximum coverages were reached, which is called a volume scan. Consequently, the lidar repeated the surveillance from the initial to last elevation angles to complete the next volume scans. A complete hemispheric range height indicator (HRHI) or RHI demonstrated that the lidar finished a scan from 0° to 180° or from 0° to 90° at a fixed azimuth angle. Although relatively dense and complete coverage of wind information (i.e., radial velocity of aerosols) were sufficiently recorded by lidar observations, the collected data are usually not located directly on the given grid points in the WISSDOM synthesis (i.e., Cartesian coordinate system). In this study, the lidar data were interpreted simply from the lidar coordinate system to the Cartesian coordinate system via bilinear interpolation.

The scanning strategy of the lidar at the DGW site includes five elevation angles for PPI (7° , 15° , 30° , 45° , and 80° before 10:00 UTC on 14 Feb. 2018 and 4° , 8° , 14° , 25° , and 80° after 10:00 UTC) and two HRHIs at azimuth angles of 51° and 330° . A full volume scan included all PPIs and HRHIs every ~ 12 min. The maximum observed radius distance is ~ 13 km, and the grid spacing is 40 m for each gate along the lidar beam. The scanning strategy of the lidar at the MHS site involves seven elevation angles for PPI (5° , 7° , 10° , 15° , 30° , 45° , and 80°) and one HRHI at an azimuth angle of 0° . A full volume scan included all PPIs and RHIs every ~ 12 min. The maximum observed radius distance was ~ 8 km, and the grid spacing was 60 m. The vertical distribution of lidar data in the test domain is shown as blue lines in Fig. 2a.

3.2.2 Automatic weather station (AWS)

Most of the AWS stations are not exactly located on the given grid points of the Cartesian



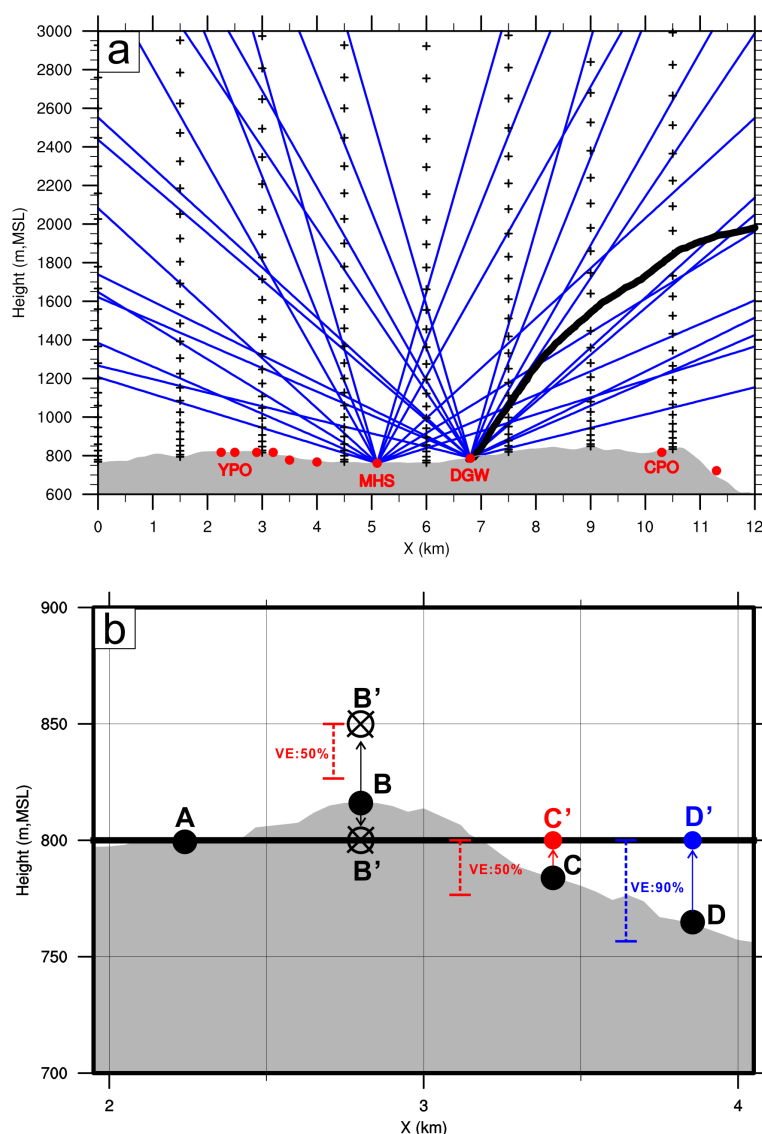
coordinate system. Objective analysis (Cressman, 1959) is a popular way to correct semirandom and inhomogeneous meteorological fields into regular grid points. This study adopted objective analysis for the AWS observations with adjustable RI distances between 100 m and 2000 m. After this first step, the observational data can reasonably interpolate to the given grid points horizontally. Furthermore, an additional step is required to put these interpolated data into the given grid points at different vertical levels because the AWSs are located at different elevations in the test domain. In the traditional way of original WISSDOM, the interpolated data are moved to the closest level with the shortest distance just above the AWS site. However, the interpolated data are NOT moved to the closest level if the shortest distances are large like more than half (50%) of grid spacing. Nevertheless, to include more data from the AWS observations appropriately, adjusted distances between the AWS sites and given grid points at different vertical levels were necessarily considered. These adjusted distances can be named as vertical extension (VE) here, and there are two options of 50% and 90% in the tests of this study, which correspond to 25 m and 45 m extensions between each grid (in case of the grid spacing is 50 m), respectively. An example demonstrated how to implement the interpolated data to the given grid points by adjustable VE after step one (Fig. 2b).

In Fig. 2b, the interpolated data do not need to move to a given grid point (as an example, at the 800 m level here) if the elevation of the AWS is equal to the height of a given grid point as point A. When the AWS is located higher than a given grid point (as point B in Fig. 2b) and does not reach the lower boundary of VE (50%) from the upper given grid point (i.e., at the 850 m level), this interpolated data will be removed and wasted. In contrast, when the interpolated data are located just below the given grid point with 50% VE, it will be achieved in the WISSDOM synthesis at the 800 m level (point C in Fig. 2b). The interpolated data of point D have a similar situation to point B; however, it will be achieved at the 800 m level because a higher VE (90%) was applied here. Since the locations of the AWS are semirandom with relatively sparse or concentrated distributions, the optimal RI and adjustable VE make it possible to include more



307 AWS observations in the WISSDOM synthesis.

308



309
 310 Figure 2. (a) Schematic diagram of the vertical distribution of adopted lidar datasets. Blue lines indicate the lidar
 311 data observed at the DGW and MHS sites with different elevation angles. The AWS stations are located on the
 312 ground and are marked by solid red circles. An example of a sounding track launched from the DGW site in one
 313 time step (06:00 UTC on 14 Feb. 2018) is plotted as a thick black line. The black cross marks indicate the vertical
 314 distribution of the LDAPS dataset. (b) Schematic diagram for data implementation with various locations of the
 315 AWS stations and different percentages of VE (vertical extension) from given grid points at the 800 m MSL
 316 level (thick black line). The gray shading on the bottom represents the topography.



317 3.2.3 Sounding

318 During ICE-POP 2018, the soundings are launched at the DGW site every 3 hours (from
319 00Z). Vertical profiles of air pressure, temperature, humidity, wind speed and directions were
320 recorded every second (i.e., ~3 m vertical spatial resolution) associated with the rising sensor.
321 The sounding sensor drifted when rising, and an example of its track in one time step is shown
322 as a thick black line in Fig. 2a. In this example, the sounding movement was mostly affected by
323 westerly winds, and it measured the meteorological parameters in any location along the track in
324 the test domain. The coordinate system of sounding data is quite similar to the distribution of
325 AWS measurements, and the observations are not located right on the given grid points of the
326 WISSDOM synthesis.

327 Similar to the AWS data, the sounding data also underwent objective analysis with an
328 adjustable RI distance for the wind measurements in the first step. Then, the interpolated data
329 were switched to given grid points for each vertical level by the different VE in the WISSDOM
330 synthesis.

331 3.2.4 Reanalysis dataset: LDAPS

332 The local reanalysis dataset LDAPS was generated by the KMA. This dataset provides u-
333 and v-component winds every 3 hours, and the horizontal spatial resolution is ~1.5 km with the
334 grid type in Lambert Conformal (as black cross marks in Fig. 1). The data revealed denser
335 distributions near the surface and sparse distributions at higher levels (see Fig. 2a). The initiations
336 of wind variables in the LDAPS were assimilated with many observational platforms, including
337 radar, AWS, satellite and sounding data. Thus, the relatively high reliability of this dataset could
338 be expected. In addition, such datasets have also significantly improved the forecast ability in
339 small-scale weather phenomena over complex terrain in Korea (Kim et al., 2019, Choi et al.,
340 2020, Kim et al., 2020).



341 The LDAPS data are not located directly on the given grid points of the WISSDOM synthesis
342 system. Unlike the distribution of AWS and sounding observations, LDAPS has dense and good
343 coverage in the test domain. Therefore, like lidar observations, the LDAPS data were also
344 interpolated to the given grid points on the Cartesian coordinate system via the bilinear
345 interpolation method.

346 **3.3 Overview of the selected strong wind event**

347 A strong wind event was selected to evaluate the performance of this newly developed
348 WISSDOM synthesis scheme. In this strong wind event, the evolution of surface wind patterns
349 on the Korean Peninsula was mainly dominated by a moving low-pressure system (LPS) which
350 is one type of strong downslope winds (Park et al, 2022, Tsai et al., 2022). The LPS moved out
351 from China and penetrated the northern part of the Korean Peninsula through the Yellow Sea
352 beginning at approximately 12:00 UTC on 13 February 2018. Consequently, a relatively strong
353 surface wind speed (exceeding $\sim 17 \text{ m s}^{-1}$) was observed when the LPS was located near the
354 northeastern coast of the Korean Peninsula ($\sim 130^\circ\text{E}$, 40°N) at 00:00 UTC on 14 February 2018
355 (Fig. 3). Then, the surface wind speed became weak when the LPS moved away from South
356 Korea after 00:00 UTC on 15 February 2018 (not shown); the details of the synoptic conditions
357 can be found in Tsai et al. (2022).

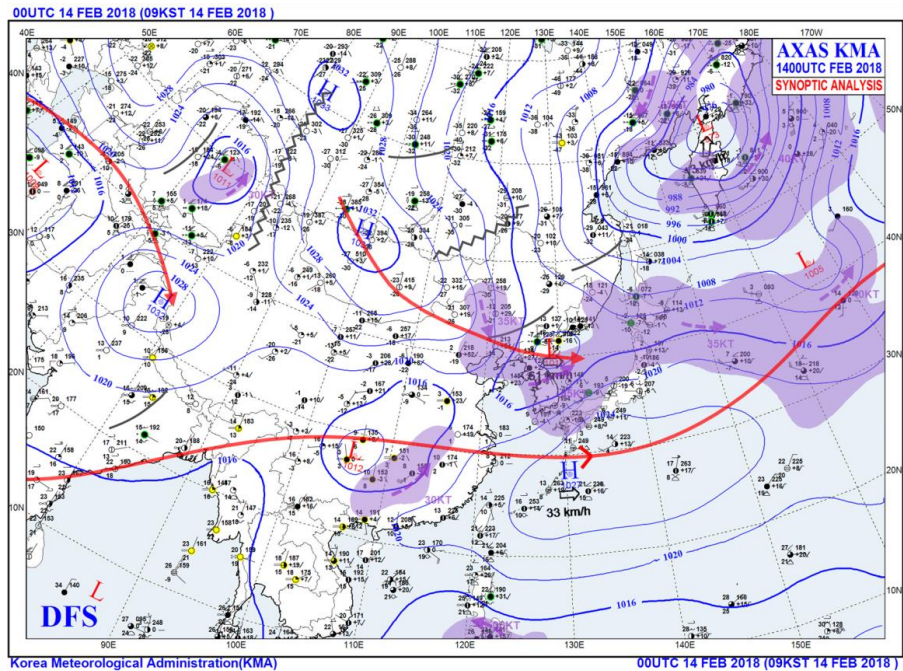


Figure 3. Synoptic surface chart from the Korea Meteorological Administration (KMA) at 00:00 UTC on 14 Feb. 2018.

This event is one of two strong wind events (i.e., daily maximum wind speeds larger than 10 m s^{-1} observed at the AWS sites along the northeastern coast of South Korea) in the past decade based on the KMA historic record. Such a strong wind event may help us to examine the potential maximum errors of the retrieved winds. Since persistent, strong westerly winds were observed by the soundings and AWS from near the surface and upper layers over the TMR during the event, the data coverages in the test domain were checked during a chosen time step (06:00 UTC on 14 February 2018). The percentage of data occupations for each dataset (after interpolation) was checked, and the results are shown in Fig. 4. Note that the elevation of the TMR is approximately 700 m MSL in the test domain. The lidars provided good coverage of 100% to 50% at the lower layers between 700 m and 800 m MSL. The coverage of lidars was reduced significantly above 900 m MSL and remained at ~5%. The maximum coverage of the AWS observations is ~40% at 800 m, and there was less coverage above this layer since relatively



few AWS stations are located in the higher mountains. Because only one sounding observation was utilized in this domain, relatively few coverages were also depicted. The local reanalysis LDAPS can provide complete coverage above 900 m MSL (exceeding 100%), albeit there was less coverage in the lower layers due to terrain. The lidar, sounding, and AWS observations covered most areas at lower levels but not higher levels; thus, the LDAPS compensated for most of the wind information at the upper layers in the WISSDOM synthesis.

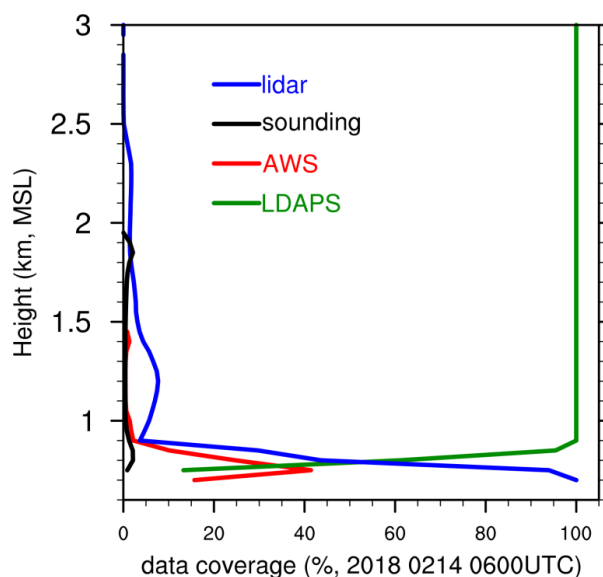


Figure 4. Data coverage (percentage, %) of the lidar (blue line), sounding (black line), AWS (red line) observations, and LDAPS (green line) at 06:00 UTC on 14 Feb. 2018.

4. Control run and the accuracy of WISSDOM

4.1 Control run

Relatively reliable 3D winds were derived by a control run of the WISSDOM synthesis because all available wind observations and local reanalysis datasets were fully acquired. These datasets provided sufficient and complete wind information with a high percentage of coverage in the test domain (cf. Fig. 4). The control run was performed carefully with the necessary



procedures in data implementation before running the WISSDOM synthesis. The lidar and LDAPS datasets must perform bilinear interpolation to the given grid points in WISSDOM, and the sounding and AWS observations must undergo objective analysis with the appropriate RI distance and VE. The quantities of the weighting coefficients for each input dataset followed the default setting from the original version of WISSDOM. The 3D winds were derived during one time step at 06:00 UTC on 14 Feb. 2018 and compared with conventional observations. The basic setting of this control run is summarized in Table 1.

Table 1 Basic setting of WISSDOM (control run)

Domain Range	Latitude: 37.606°N~37.713°N Longitude: 128.642°E~128.778°E
Domain Size	12 × 12 × 3 km (long × width × vertical)
Spatial Resolution	0.05 × 0.05 × 0.05 km (long × width × vertical)
Terrain Resolution	0.09 km
Coordinate System	Cartesian coordinate system
Background	Sounding (DGW)
Data Implementation	Doppler Lidars (MHS, DGW): bilinear interpolation AWS: objective analysis (RI*: 1 km, VE*: 90%) Sounding (DGW): objective analysis (RI: 1 km, VE: 90%) LDAPS: bilinear interpolation
Weighting Coefficient (input datasets)	Doppler Lidars (α_1): 10^6 Background (α_2): 10^2 Sounding (α_6): 10^6 AWS (α_7): 10^6 LDAPS (α_8): 10^3

*RI: radius influence, VE: vertical extension

The results of 3D winds at 800 m MSL derived from the control run are shown in Figs. 5a, c, and e. Topographic features comprised relatively lower elevations in the center of the test domain, and there were weaker u-component winds ($\sim 7 \text{ m s}^{-1}$) near the AWSs and MHS lidar sites between 128.67°E and 128.71°E (Fig. 5a). In contrast, the u-component winds ($\sim 15 \text{ m s}^{-1}$) were almost doubled near the DGW lidar site (between 128.71°E and 128.73°E). The vertical structures of the u-component winds across these two lidars (i.e., along the black line in Fig. 5a)



402 are shown in Fig. 5b. The strength of the u-component winds rapidly increased from the surface
403 to the upper layers (from ~ 6 to 20 m s^{-1}), and uniform u-component winds with wavy pattern
404 were depicted above $\sim 1 \text{ km MSL}$ except for the stronger winds near the surface surrounding the
405 DGW site. There were relatively weak (strong) u-component winds surrounding the lidar at the
406 MHS (DGW) site near the surface. Relatively weak v-component winds were found
407 (approximately $\pm 4 \text{ m s}^{-1}$) at 800 m MSL (Fig. 5c); thus, the horizontal wind directions were
408 mostly westerly winds during this time step. The v-component winds were obviously accelerated
409 in several local areas encompassing the terrain (near 128.71°E). The vertical structure of the v-
410 component winds (Fig. 5d) indicates that the v-component winds became stronger in the upper
411 layer. The wind directions were changed from westerly to southwesterly from the near surface
412 up to $\sim 1.4 \text{ km MSL}$ height. Updrafts were triggered on windward slopes when westerly winds
413 impinge the terrain or hills (Figs. 5e and 5f). Basically, the 3D winds derived from the WISSDOM
414 synthesis reveal reasonable patterns compared to synoptic environmental conditions (cf. Fig. 3);
415 the moving LPS accompanied stronger westerly winds.

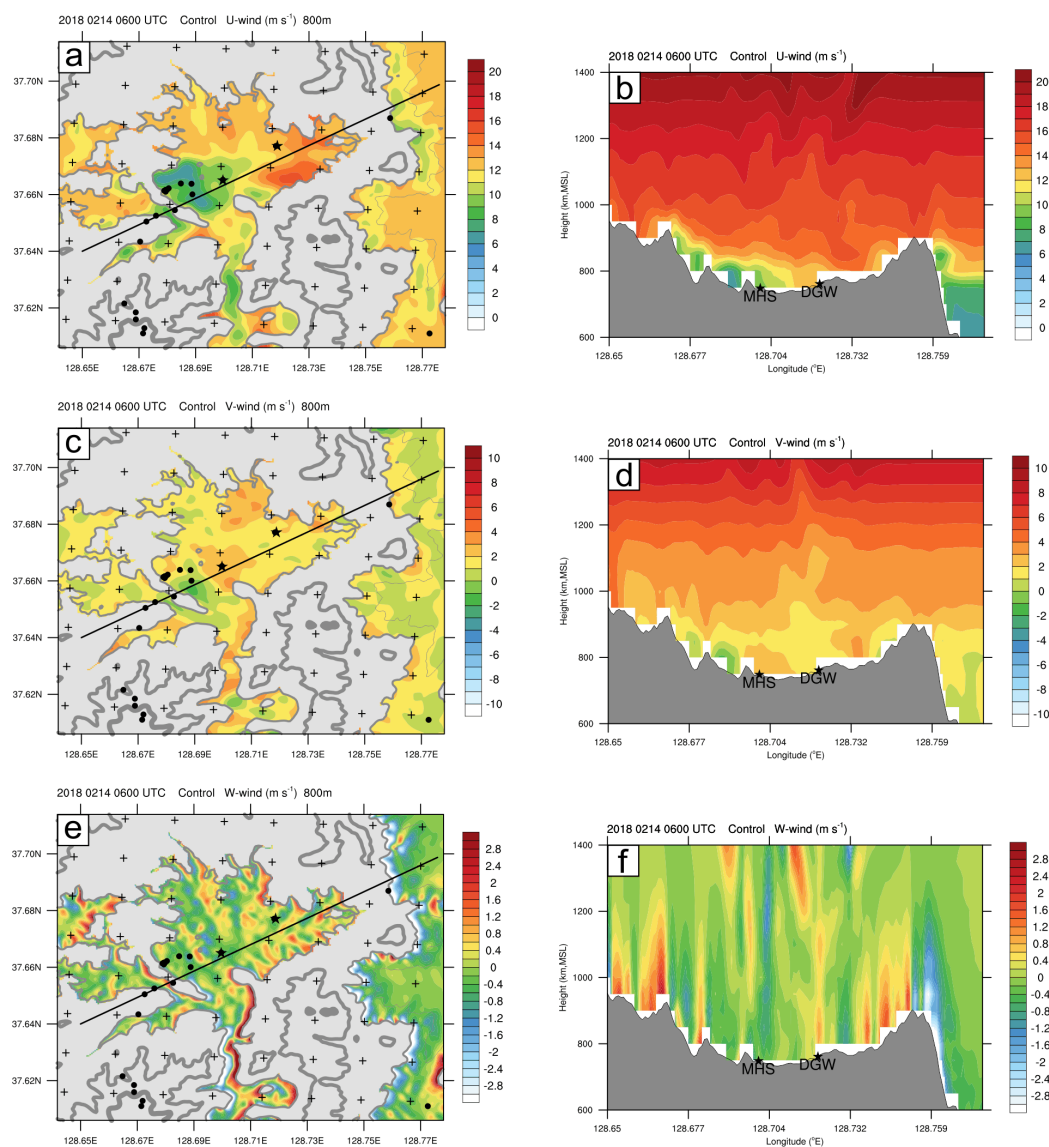


Figure 5. The 3D winds were derived from the control run by the WISSDOM synthesis at 06:00 UTC on 14 Feb. 2018. (a) The u-component winds (color, m s^{-1}) at 800 m MSL; the gray shading represents the terrain area, and the contours indicate different terrain heights of 600 m, 800 m and 1000 m MSL corresponding to thin to thick contours. The locations of lidars are marked with asterisks. (b) Vertical structures of u-component winds (color, m s^{-1}) along the black line in (a). The gray shading in the lower part of the figure indicates the height of the terrain. (c) and (d) are the same as (a) and (b) but for the v-component winds. (e) and (f) are the same as (a) and (b) but for the w-component winds.



424 **4.2 Intercomparison between derived winds and observations**

425 Detailed analyses were performed in this section to quantitatively evaluate the accuracy of
426 the derived 3D wind from the WISSDOM synthesis. Two kinds of instruments were available in
427 the test domain to detect the relatively realistic winds: sounding and lidar quasi-vertical profiles
428 (QVP, Ryzhkov et al., 2016). The horizontal winds observed from soundings and the 3D winds
429 of the lidar QVP were utilized to represent observations. A complete analysis of the
430 intercomparison between the WISSDOM synthesis and observations is presented in the following
431 subsections.

432 **4.2.1 Sounding**

433 The discrepancies in horizontal winds derived from WISSDOM and the sounding
434 observations for the entire research period (from 12:00 UTC on 13 to 12:00 UTC on 14 February
435 2018) were analyzed. Fig. 6 shows the scatter plots of the u- and v-component winds on the
436 locations following the tracks of sounding launched from the DGW site. Most of the u-component
437 winds derived from WISSDOM are in good agreement with the sounding observations, and the
438 wind speed is increased with the height from approximately 10 to 40 m s⁻¹. Slight underestimation
439 of retrieved u-component winds can be found at the layers of 1.5~2 km MSL (Fig. 6a). In contrast,
440 most of the v-component winds were weak (smaller than 15 m s⁻¹) at all layers, because the
441 environmental winds were more like westerlies during the research period. There were also
442 slightly overestimated v-component winds derived from WISSDOM at the layers of 1.5~2 km
443 MSL (Fig. 6b). The possible reason why the overestimated winds occurred above ~1.5 km MSL
444 is that lidar data had relatively less coverages at higher layers (cf. Fig. 4).

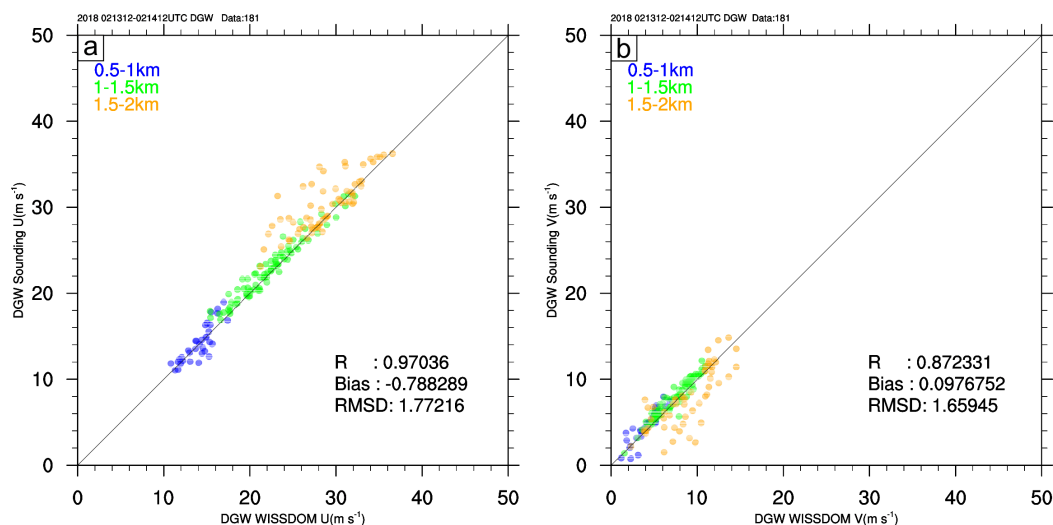
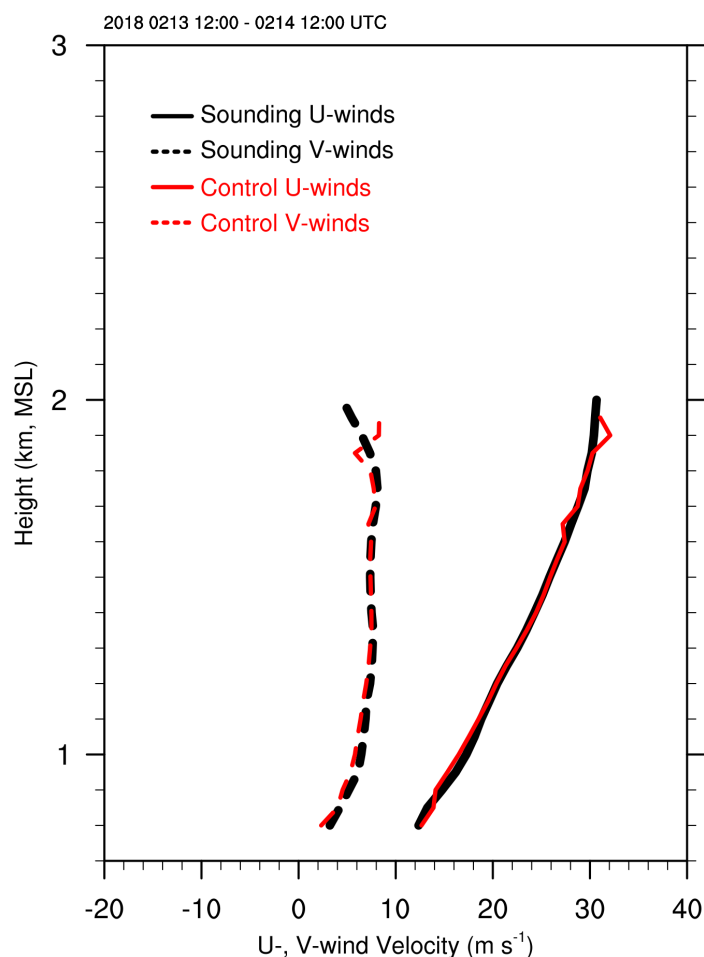


Figure. 6. Scatter plots of (a) u-component winds between the WISSDOM synthesis (x-axis) and sounding observations (y-axis) above the DGW site during the research period. The colors indicate different layers, and the numbers of data points, correlation coefficients, average biases and root mean square deviations are also shown in the figure. (b) The same as (a) but for v-component winds.

Overall, the u-component winds show a high correlation coefficient (exceeding 0.97), low average bias (-0.78 m s^{-1}), and the root mean square deviation (RMSD) of 1.77 m s^{-1} . The correlation coefficient of the v-component is also high (0.87), the average bias is 0.09 m s^{-1} , and the RMSD is 1.65 m s^{-1} .



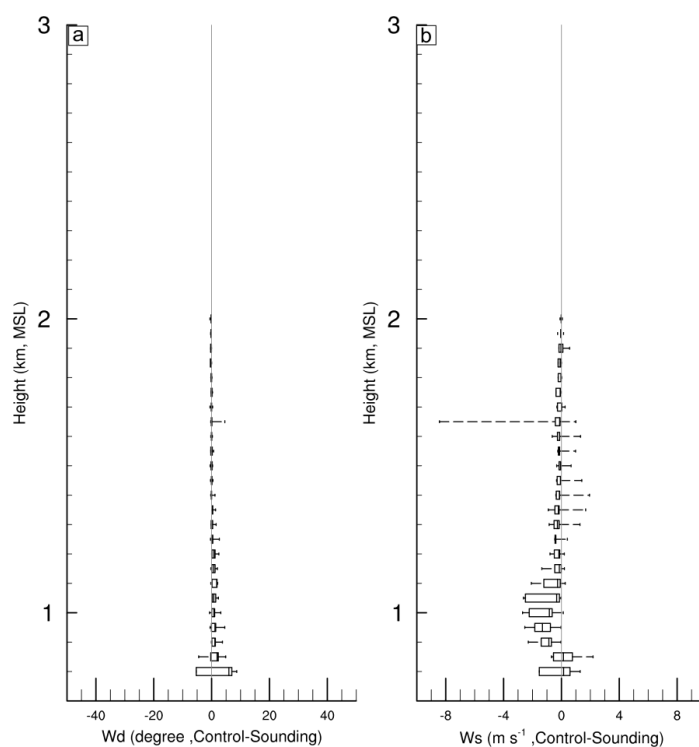
454
 455 Figure 7. Vertical wind profiles of average horizontal winds derived from the WISSDOM synthesis (red lines and
 456 vectors) and sounding observations (black lines and vectors) above the DGW site from 12:00 UTC on 13 to
 457 12:00 UTC on 14 Feb. 2018. Solid lines indicate u-component winds (m s^{-1}), and dashed lines indicate v-
 458 component winds (m s^{-1}).

459 The vertical profiles of the averaged u- and v-component winds for the period of 12:00 UTC
 460 on 13 to 12:00 UTC on 14 Feb. 2018 are shown in Fig. 7 for the WISSDOM synthesis (red) and
 461 sounding observations (black) launched from the DGW site. The average profiles agree well
 462 except for the height above 1.5 km MSL, slight discrepancies of u- and v-component winds (< 1
 463 m s^{-1}). Their statistical errors during the entire research period were quantified by the box plot
 464 shown in Fig. 8.



465 The maximum difference in wind directions between the WISSDOM synthesis and sounding
 466 observations is small at all layers. The interquartile range (IQR) and median values of the wind
 467 direction are also smaller (between ~ 0 and 2.5 degrees) except for relatively larger IQR existed
 468 (between ~ -5 and 5 degrees) and larger median values (between ~ 0 and 5 degrees) at the lowest
 469 level during the entire research period (Fig. 8a). Basically, the IQR and median values of the
 470 wind direction are close to 0 degrees above 1 km MSL. Fig. 8b shows the difference in wind
 471 speed between the WISSDOM synthesis and sounding observations. The wind speed derived
 472 from WISSDOM was slightly underestimated in the layers between ~ 0.85 and 1.3 km MSL. The
 473 median values of the wind speed were between -1 and 0.5 m s^{-1} , and the IQR of wind speed was
 474 between -2 and 0.5 m s^{-1} . Above 1.3 km MSL, the differences in wind speed are small as their
 475 median values are close to 0 m s^{-1} .

476



477 Figure 8. The box plot of average (a) wind direction discrepancies between the WISSDOM synthesis and sounding
 478 observations above the DGW site during the research period. (b) Same as (a) but for the wind speed.
 479



4.2.3 Lidar QVP

The lidar QVP is another observational reference used to evaluate the performance of derived winds from the WISSDOM synthesis. The scatter plots of the horizontal winds derived from WISSDOM and lidar QVP at the DGW site are shown in Fig. 9. The strength of the u-component winds increases with height in the range between approximately 10 m s^{-1} and 40 m s^{-1} from the surface up to $\sim 2.5 \text{ km}$ MSL (Fig. 9a). Although the results show a relatively high correlation coefficient (0.84) for the u-component winds from lower to higher layers in the entire research period, the degree of scatter is larger than that in Fig. 6a. The average bias and RMSD of the u-component winds are 2.83 m s^{-1} and 3.69 m s^{-1} , respectively. The correlation coefficient of v-component winds is lower (0.35) in association with low wind speed ($< 15 \text{ m s}^{-1}$) from the surface to 2.5 km MSL (Fig. 9b). The average bias and RMSD of the v-component winds are 2.26 m s^{-1} and 2.92 m s^{-1} , respectively. The results of these scatter plot analyses are summarized in Table 2. Basically, the u-component winds have high correlations, relatively lower bias, and lower RMSD than the v-component winds because the environmental winds are more westerly.

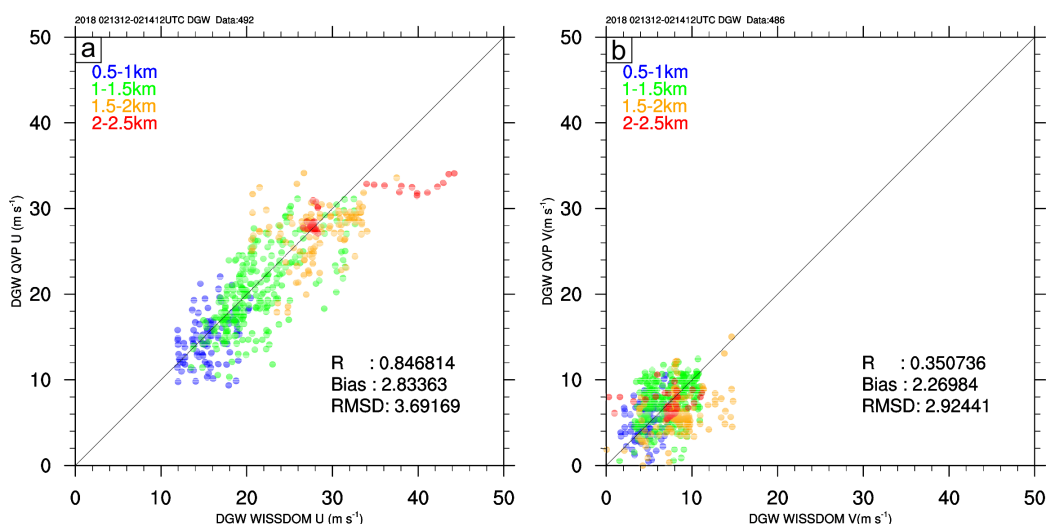


Figure 9. The same as Fig. 6 but for (a) u-component winds between the WISSDOM synthesis (x-axis) and lidar QVP (y-axis). (b) The same as (a) but for v-component winds.



Table 2 Summary of the intercomparisons between WISSDOM and observations

		Correlation coefficient	Average bias (m s^{-1})	RMSD (m s^{-1})
WISSDOM-sounding	u-component	0.97	-0.78	1.77
	v-component	0.87	0.09	1.65
WISSDOM-lidar QVP	u-component	0.84	2.83	3.69
	v-component	0.35	2.26	2.92

498 Compared to the sounding observations, additional w-component winds are available in
 499 lidar QVP, which allows us to check their discrepancies in 3D winds. However, most of the
 500 vertical velocity observations were quite weak (approximately $\pm 0.2 \text{ m s}^{-1}$) above the DGW site,
 501 and relatively low reliability of the derived vertical velocity could be expected in this event.
 502 Therefore, the average vertical profiles of 3D winds were utilized to qualitatively check the
 503 discrepancies between WISSDOM synthesis and lidar QVP during the research period (Fig. 10).
 504 The results show that the average u-component winds have relatively smaller discrepancies
 505 (approximately $< 1 \text{ m s}^{-1}$) between the WISSDOM synthesis (marked as WISS-U in Fig. 10) and
 506 lidar QVP (marked as QVP-U) below $\sim 1.3 \text{ km}$ MSL at the DGW site. In contrast, there were
 507 larger discrepancies (approximately $> 2 \text{ m s}^{-1}$) between 1.3 km and 2 km MSL. The average v-
 508 component winds derived from WISSDOM (marked as WISS-V) and lidar QVP (QVP-V) were
 509 generally weak, and the ranges of WISS-V and QVP-V were between $\sim 2 \text{ m s}^{-1}$ and 8 m s^{-1} .
 510 Generally, the vertical profiles of WISS-V were nearly overlain with QVP-V, and their
 511 discrepancies existed in the height range $1.6\sim 2.0 \text{ km}$ MSL (maximum $\sim 4 \text{ m s}^{-1}$). Smaller (larger)
 512 discrepancies of w-component winds were significantly below (above) the height at $\sim 1.3 \text{ km}$
 513 MSL (maximum discrepancies $\sim 0.6 \text{ m s}^{-1}$ at 1.7 km MSL). Despite the larger discrepancies, the
 514 similar patterns of W can also be shown. In summary, the discrepancies in the 3D winds between
 515 the WISSDOM synthesis and lidar QVP were small in the lower layers and large in the higher
 516 layers because the observational data from lidars and AWSs provided good quality and sufficient
 517 wind information at the lower layers but not in the higher layers (lower coverages of lidar data
 518 above 1.3 km MSL, cf. Fig. 4).

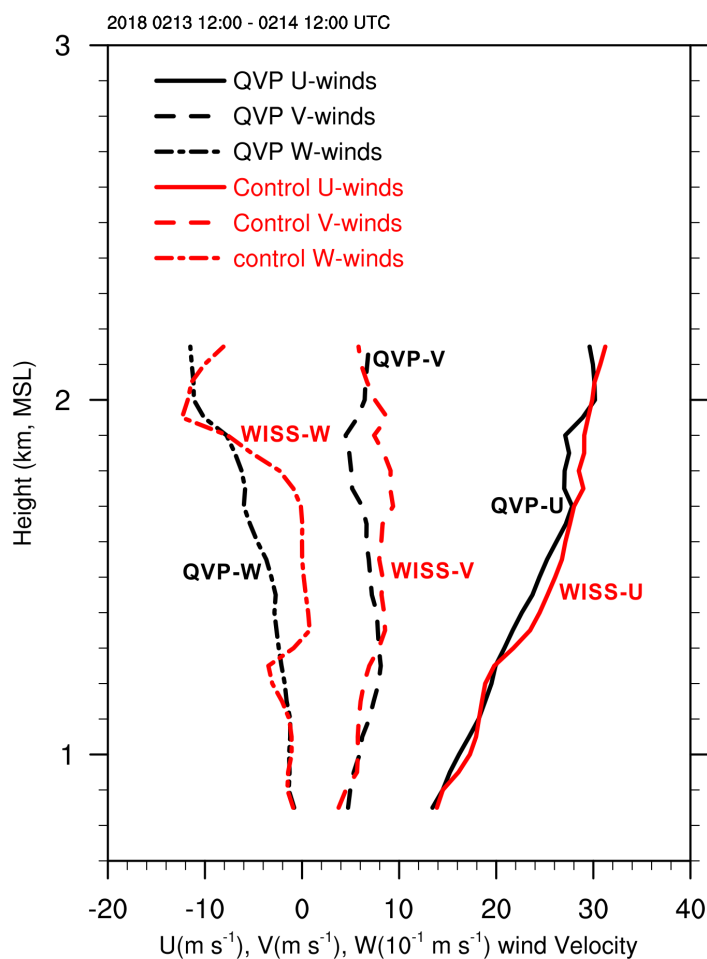


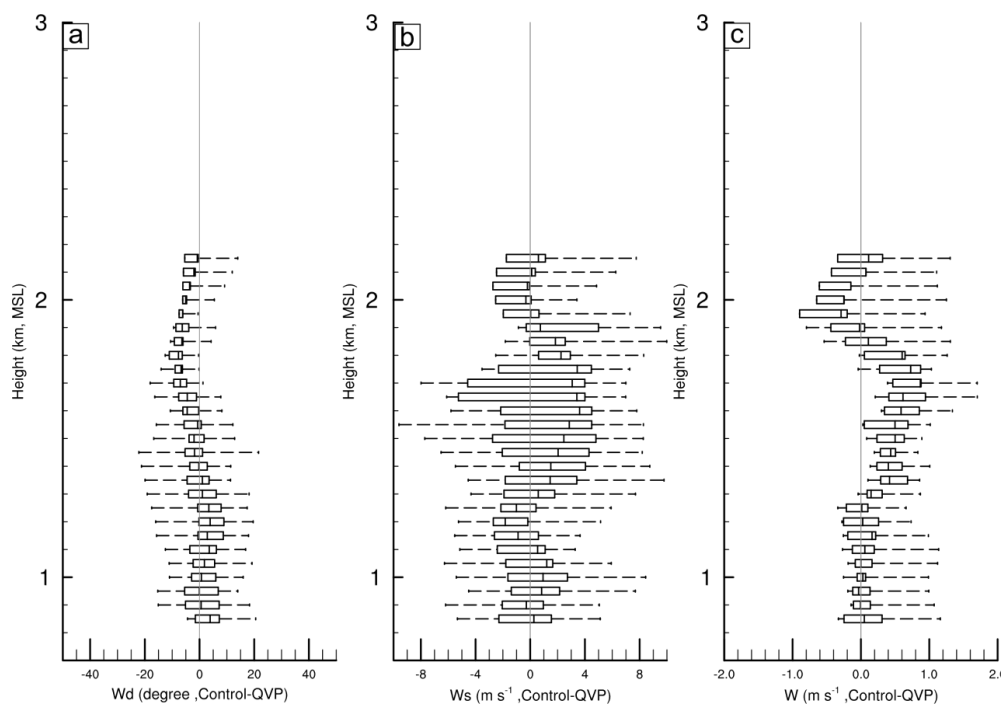
Figure 10. Vertical wind profiles of average 3D winds derived from the WISSDOM synthesis (red lines and vectors) and lidar QVP (black lines and vectors) above the DGW site from 12:00 UTC on 13 to 12:00 UTC on 14 Feb. 2018. Solid lines indicate u-component winds (m s⁻¹), dashed lines indicate v-component winds (m s⁻¹), and dash-dotted lines indicate w-component winds (10⁻¹ m s⁻¹). The u-, v-, and w-component winds derived from the WISSDOM synthesis (lidar QVP) were marked by WISS-U (QVP-U), WISS-V (QVP-V), and WISS-W (QVP-W), respectively.

Fig. 11 shows the quantile distribution of statistical errors of wind direction, wind speed and vertical velocity between the WISSDOM synthesis and lidar QVP during the research period. The IQR of the wind direction is smaller (−5~5 degrees) in the layers from 0.85 km to 1.5 km MSL and turns to approximately −10~0 degrees above 1.5 km MSL. The median values of wind direction are smaller −5~5 degrees) from near the surface to the upper layers (Fig. 11a). Fig. 11b



531 shows that the median values (IQR) of wind speed are approximately $-1\sim1\text{ m s}^{-1}$ ($-2\sim2\text{ m s}^{-1}$)
532 below 1.5 km MSL, and they all become larger with heights above 1.5 km MSL (between -1 and
533 3 m s^{-1} for median values and $-4\sim4\text{ m s}^{-1}$ for the IQR). The statistical error of the vertical velocity
534 reveals that the IQR is $-0.2\sim0.2\text{ m s}^{-1}$ ($-0.8\sim0.8\text{ m s}^{-1}$) below (above) 1.3 km MSL, and the
535 median values are $0\sim0.2\text{ m s}^{-1}$ ($-0.2\sim0.6\text{ m s}^{-1}$) below (above) 1.3 km MSL. The results of
536 statistical errors are summarized in Table 3.

537



538

539

540

541

542

543

544

545

546

547

Figure 11. The box plot of average (a) wind direction discrepancies between the WISSDOM synthesis and sounding observations above the DGW site during the research period. (b) Same as (a) but for the wind speed. (c) Same as (a) but for the w-component winds.



Table 3 Summary of the statistical errors between WISSDOM and observations

		Interquartile range (IQR)	Median values
WISSDOM-sounding	wind direction	0~2.5 (deg.)	0~2.5 (deg.)
	wind speed	-2~0.5 (m s ⁻¹)	-1~0.5 (m s ⁻¹)
WISSDOM-lidar QVP	wind direction	-10~5 (deg.)	-5~5 (deg.)
	wind speed	-4~4 (m s ⁻¹)	-1~3 (m s ⁻¹)
	w-component winds	-0.8~0.8 (m s ⁻¹)	-0.2~0.6 (m s ⁻¹)

548 5. Sensitivity test with various datasets, data implementation and weighting coefficients

549 5.1 Impacts of various datasets (Experiment A)

550 In this session, the impacts of various datasets implemented in the WISSDOM synthesis were
 551 evaluated. The basic setting of Experiment A is the same as that of the WISSDOM control run
 552 (cf. Table 1) except for four designs in Experiment A. The details of these four designs are
 553 summarized in Table 4 as the control run without the lidar observations (A-1), the control run
 554 without the AWS observations (A-2), the control run without the sounding observations (A-3)
 555 and the control run without the LDAPS data (A-4). The discrepancies of 3D winds were examined
 556 between the control run and each design in Experiment A. Since the environmental wind speed
 557 is nearly comprised of uniform westerlies in this event, the results only show the difference in u-
 558 component winds between control run and each design (A-1~A-4) in Fig. 12.

559 Fig. 12a reveals the discrepancies in horizontal u-component winds at 800 m MSL as the A-
 560 1 is subtracted from the control run. This result reflects the impacts of lidar observations on the
 561 u-component winds in the WISSDOM synthesis. The most significant contributions from the
 562 lidar observations are the high wind speed existing near the DGW site in a relatively narrow



valley. The mechanisms of the accelerated wind speed due to the channeling effect in this local area were verified by our previous study (Tsai et al. 2022). The lidar observations also contributed to the high wind speed in another area near the western side of the MHS site (128.68°E, 37.66°N). Based on the analysis in the vertical cross section of u-component winds in A-1 (Fig. 12b), the lidar observations significantly affected the high wind speed only in the lower levels (below ~900 m MSL) but not in the higher levels. Lidar observations provided sufficient coverage only for lower levels and not higher levels (cf. Fig. 4).

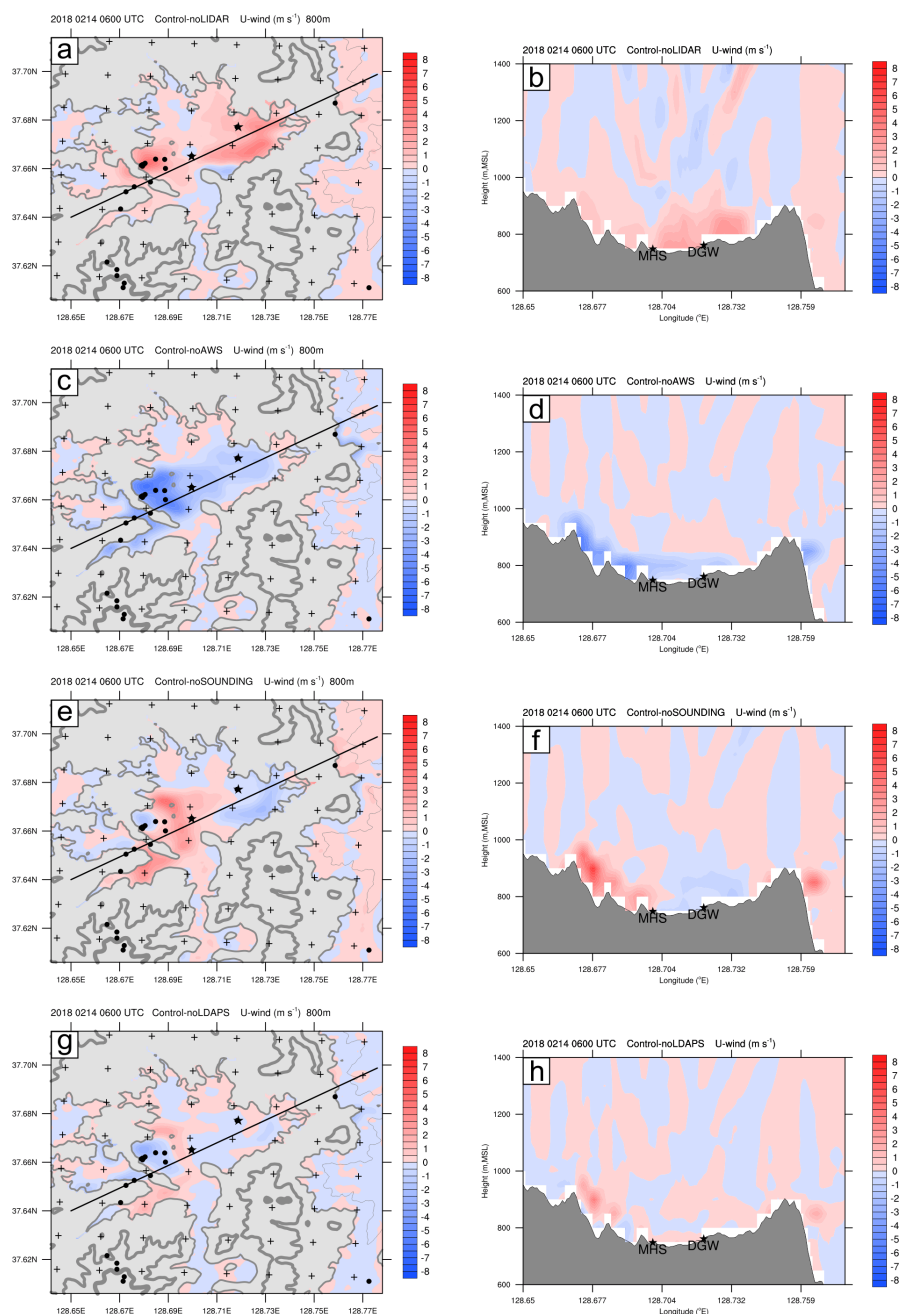
Table 4 Experiment setting (sensitivity testing)

	Various datasets	Including Doppler lidars, AWSs, Soundings, LDAPS	
Control run	Interpolation of AWS	RI: 1.0 km, VE: 90%	
	Weighting Coefficient	AWS (α_7): 10^6 Doppler Lidars (α_1): 10^6 LDAPS (α_8): 10^3	
Experiment A	Various datasets	A-1	Excluding Doppler Lidars
		A-2	Excluding AWSs
		A-3	Excluding Soundings
		A-4	Excluding LDAPS
Experiment B	Interpolation of AWS	B-1	RI: 0.5 km, VE: 50%
		B-2	RI: 0.5 km, VE: 90%
		B-3	RI: 1.0 km, VE: 50%
		B-4	RI: 2.0 km, VE: 50%
		B-5	RI: 2.0 km, VE: 90%
Experiment C	Weighting Coefficient (constraints)	C-1	AWS (α_7): 10^3
		C-2	Doppler Lidars (α_1): 10^3
		C-3	LDAPS (α_8): 10^6

The AWSs have negative impacts on the u-component winds in most areas at 800 m MSL in A-2 (Fig. 12c), especially in the western areas of the MHS site. Negative contributions of the u-component winds produced by the AWS observations were restricted near the surface, and the low wind speed area was extended to ~100 m above the surface (Fig. 12d). The contributions of



the u-component winds from the sounding observations were weak near the DGW sounding site
 in A-3 (Figs. 12e and 12f). The impacts of u-component winds from the LDAPS datasets were
 rather smaller in most of analysis area. in A-4 (Figs. 12g and 12h).



579



580 Figure 12. (a) The discrepancies in horizontal u-component winds between the control run and A-1 at 800 m MSL
 581 at 06:00 UTC on 14 Feb. 2018. (b) The same as (a) but for the vertical section along the black line in (a). (c) and
 582 (d) are the same as (a) and (b) but for A-2. (e) and (f) are the same as (a) and (b) but for A-3. (g) and (h) are the
 583 same as (a) and (b) but for A-4.

584 Averaged discrepancies of derived 3D winds for each vertical level are shown in Fig. 13.
 585 These results summarized a series of sensitivity tests if the WISSDOM synthesis lacks certain
 586 data inputs (i.e., A-1~A-4 in Experiment A) for derived u-, v- and w-component winds in the test
 587 domain. Overall, the maximum absolute value of averaged discrepancies for Experiment A are
 588 smaller than approximately 0.5 m s^{-1} , which are the discrepancies of the u-component winds for
 589 A-1 and A-2 located at 800 m MSL. Except for these values, the values of the derived u-, v- and
 590 w-component winds for A-1~A-2 are approximately smaller than 0.2 m s^{-1} from the surface up
 591 to the top in the test domain.

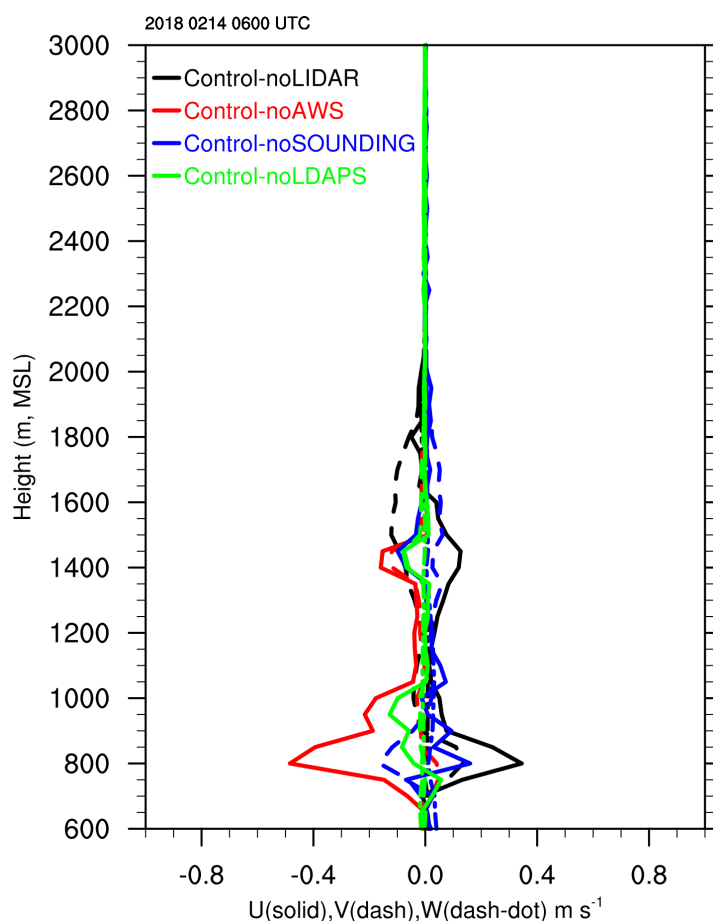


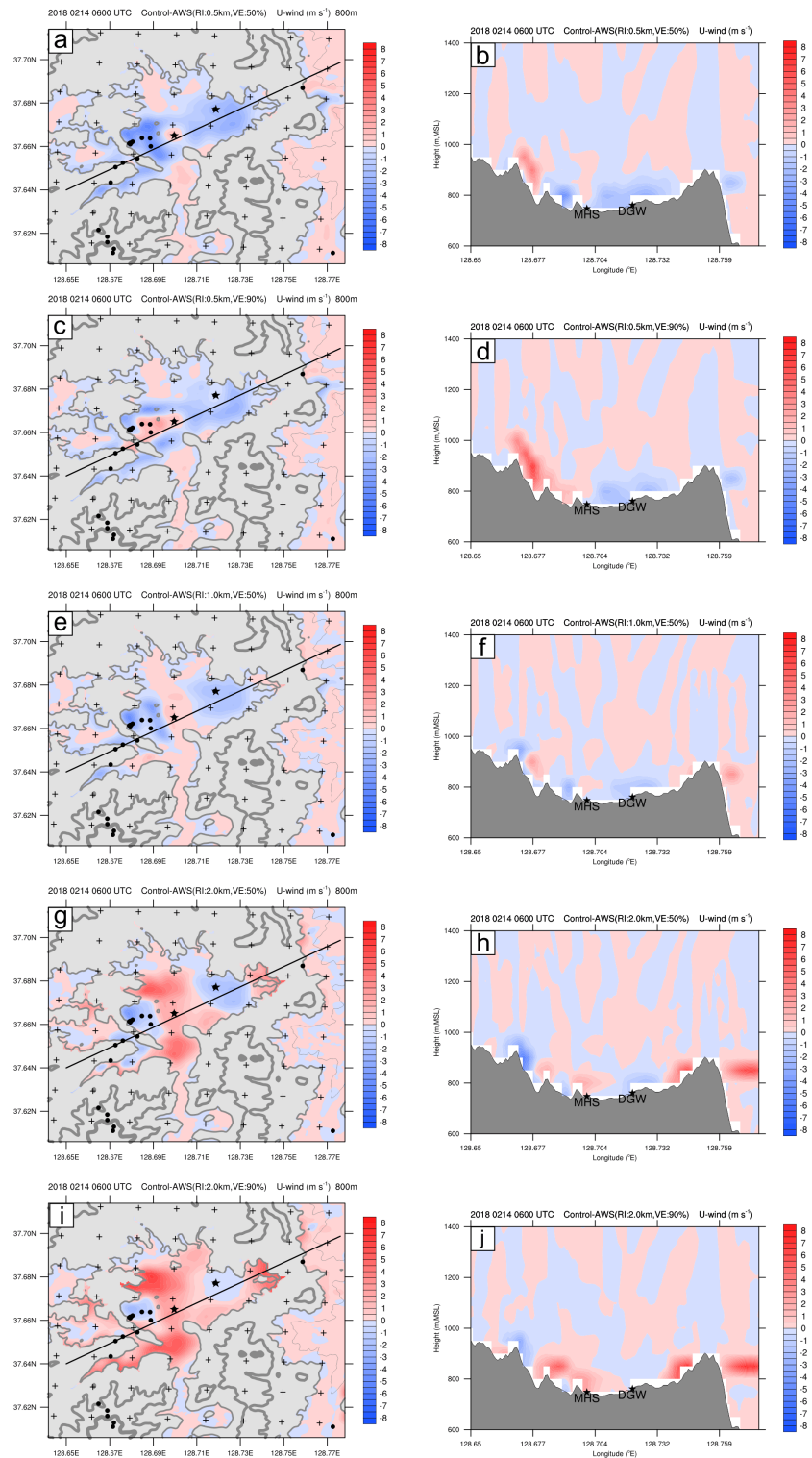
Figure 13. Vertical profiles of averaged discrepancies of 3D winds for each design in Experiment A at 06:00 UTC on 14 Feb. 2018. The averaged discrepancies of u-, v- and w-component winds were plotted by solid, dash, and dash-dot lines, and the black, red, blue and green lines indicate A-1, A-2, A-3 and A-4, respectively.

5.2 Radius of influence (RI) and vertical extension for the AWS (Experiment B)

Experiment B was performed to check the discrepancies in 3D winds between the control run and the different settings of RI and VE with the AWS observations. There were five designs (B-1~B-5) in Experiment B with the ranges of RI (VE) between 0.5 km (50%) and 2 km (90%). The details are shown in Table 4. The horizontal u-component winds at 800 m MSL and the vertical structure of Experiment B at one time step (06:00 UTC on 14 February 2018) are shown in Fig. 14. An unusual circular area with positive discrepancies around the MHS site was depicted in B-



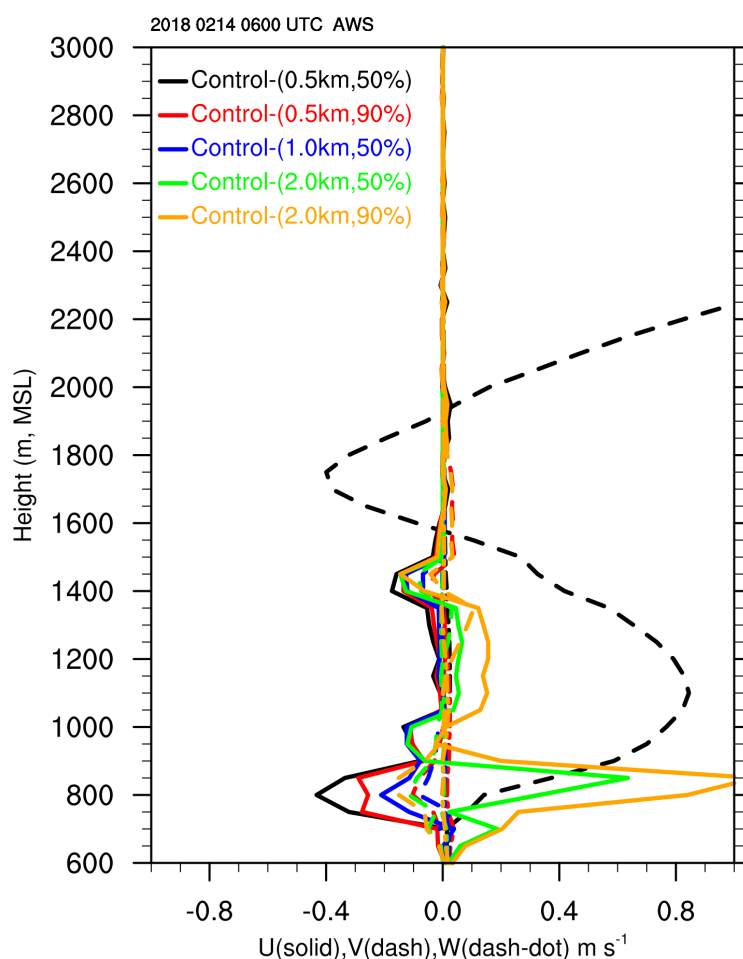
603 1 (Figs. 14a and 14b), which may have been produced by the insufficient RI distance and VE.
604 Relatively smaller RI and VE values can only include relatively less wind information if the
605 distances between AWS stations are large. Enlarging the RI and VE are required to appropriately
606 include more wind information from the AWS observations. Figs. 14c and 14d show the results
607 of B-2 as VE reached 90%. Although the unusual circle vanished, there were discontinuities with
608 negative values near the northern and southern areas of the MHS site and positive areas
609 surrounding the AWSs (128.68°E, 37.66°N). The setting of B-3 was similar to that of the control
610 run except that the VE was 50%. The discrepancies were relatively small, albeit dense AWS
611 stations contributed even smaller negative values in the western areas of the MHS sites (Figs. 14g
612 and 14h). Obviously, positive discrepancies appeared near the northern and southern areas of the
613 MHS site in B-4 and B-5 (Figs. 14g-j). The impacts of the AWS with various settings (B-1~B-5)
614 on the discrepancies in u-component winds were both restricted near the surface, even with a
615 larger RI and high VE.





617 Figure 14. The same as Fig.12, but (a) and (b) for B-1. (c) and (d) are the same as (a) and (b) but for B-2. (e) and (f)
 618 are the same as (a) and (b) but for B-3. (g) and (h) are the same as (a) and (b) but for B-4. (i) and (j) are the same
 619 as (a) and (b) but for B-5.

620 Fig. 15 shows the vertical profiles of averaged discrepancies of derived 3D winds in
 621 Experiment B. This figure summarizes the results of sensitivity testing with different settings of
 622 the RI and VE in WISSDOM (i.e., B-1~B-5 in Experiment B, shown in Table 4) for derived u-,
 623 v- and w-component winds in the test domain. The maximum discrepancies of u-component
 624 winds in B-1, B-2 and B-3 were quite small at only 0.4, 0.3 and 0.2 m s⁻¹, respectively.
 625 Nevertheless, the maximum discrepancies of u-component winds for B-4 and B-5 were larger
 626 than 0.6 m s⁻¹ and even exceeded ~1 m s⁻¹. Although the discrepancies in the u-component winds
 627 in B-1 were small, the discrepancies in the v-component winds in B-1 reveal unusual patterns,
 628 with larger positive values at ~1100 m MSL and negative values at ~1800 m MSL (black dashed
 629 line in Fig. 15), the possible reason is the minimizations of cost function are not converged well
 630 because relatively few and weak v-component winds were included in B-1. Except for this value,
 631 the maximum discrepancies of v-component winds were small for B-2~B-5, and the maximum
 632 discrepancies of w-component winds were also small for all of Experiment B. Note that B-3
 633 always has the smallest discrepancies with the derived 3D winds because the setting is quite
 634 similar to the control run.



635

636 Figure 15. The same as Fig. 13. but for B-1~B-5.

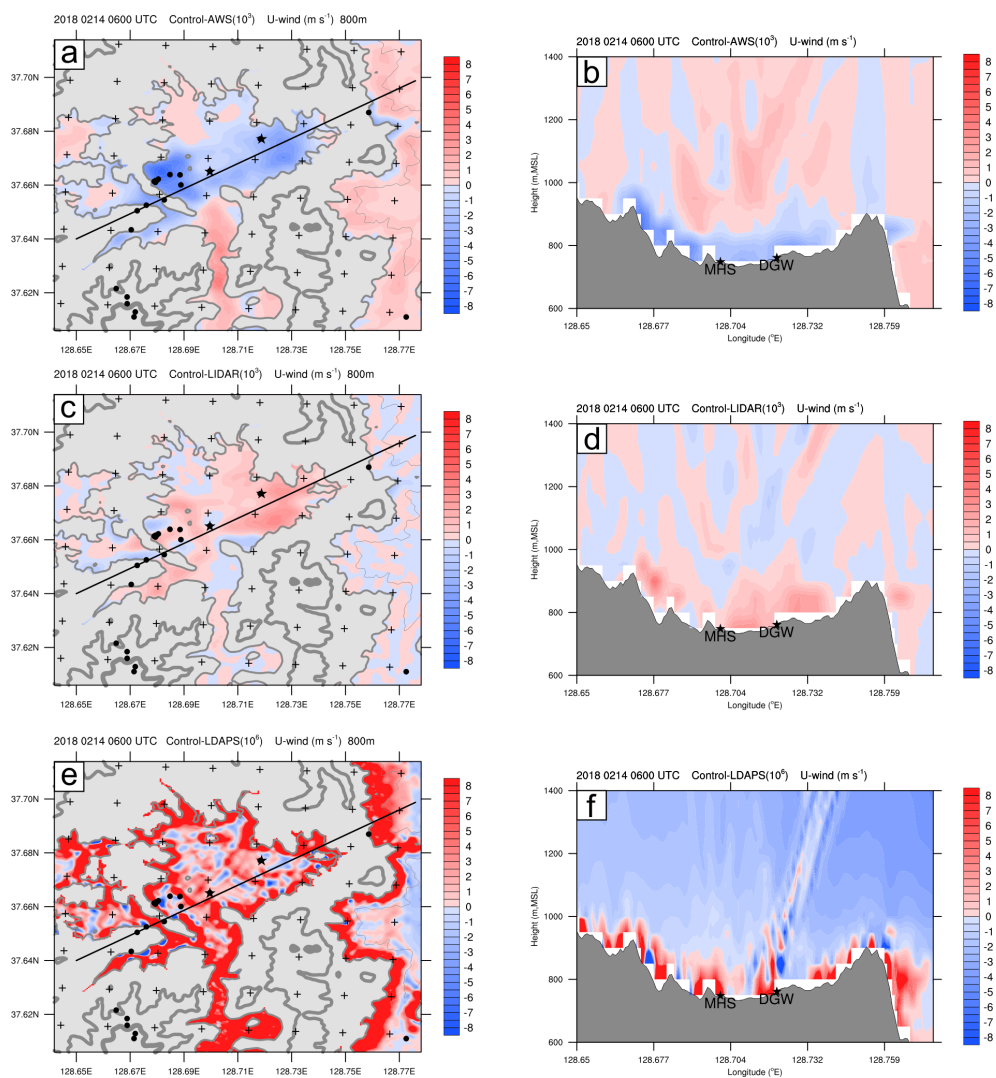
637 5.3 Different weighting coefficients for the constraints (Experiment C)

638 Experiment C was designed to check the discrepancies in the derived u-component winds
 639 between the control run and experimental runs with different weighting coefficients for each
 640 constraint related to the AWS, lidar and LDAPS (corresponding to C-1, C-2 and C-3 in Table 4).
 641 Originally, the weighting coefficients for the AWS and lidar observations were set to 10^6 , and the
 642 value was 10^3 for the LDAPS dataset (i.e., control run, Table 1). The results of Experiment C
 643 show significant negative discrepancies in u-component winds near the surface in C-1, especially

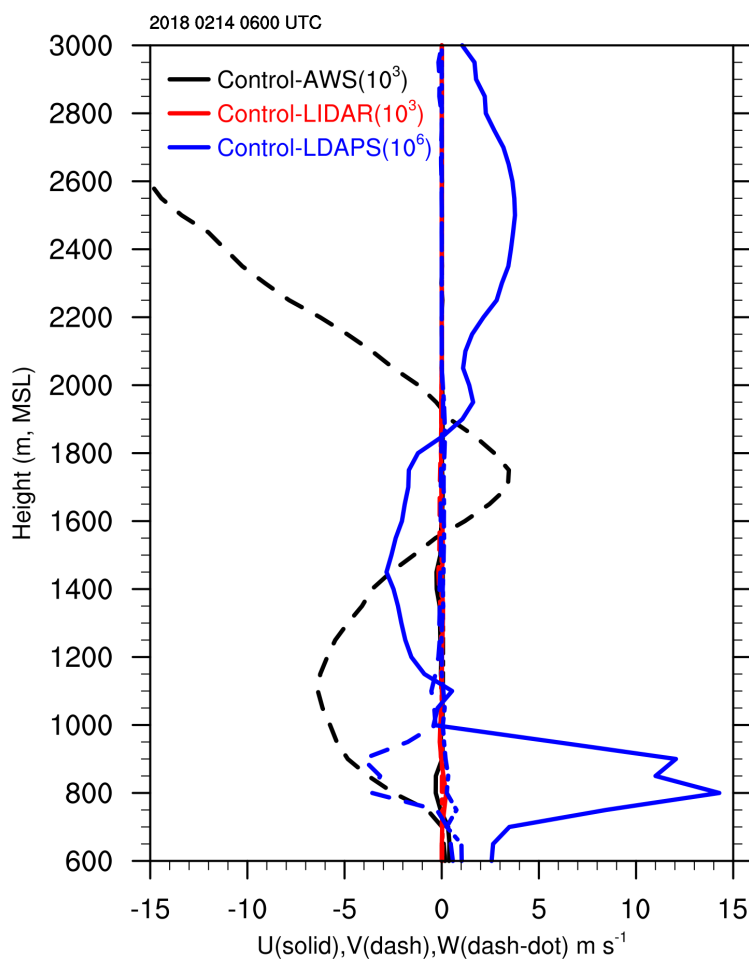


in the areas next to the AWSs (128.68°E, 37.66°N). The discrepancies for C-1 (Figs. 16a and 16b) and C-2 (Figs. 16c and 16d) are similar to those for A-2 (Figs. 12c and 12d) and A-1 (Figs. 12a and 12b), respectively. The inputs of AWSs and lidar both contributed relatively weak impacts to the WISSDOM synthesis when the weighting coefficient was set to 10^3 . Irrational patterns were depicted when the weighting coefficient of LDAPS inputs increased to 10^6 , and larger and positive discrepancies were crowded into most areas in the valley (i.e., C-3, Figs. 16e). Larger and positive discrepancies existed only near the surface, and there were negative discrepancies between approximately 1000 m and 1400 m (Fig. 16f). Note that the influences of sounding observations also existed above the DGW site in scenario C-3.

The vertical profiles of averaged discrepancies of derived 3D winds in Experiment C are shown in Fig. 17. Absolute values of the discrepancies in the u-, v- and w-component winds are smaller than 1 m s^{-1} , except for the discrepancies in the v-component winds with low weighting of the AWS observations (i.e., C-1) and the discrepancies in the u- and v-component winds with the high weighted LDAPS (i.e., C-3). The discrepancies in the v-component winds in C-1 exceeded -5 m s^{-1} at $\sim 1100 \text{ m MSL}$ and were larger than -15 m s^{-1} above 2600 m MSL . These unreasonable characteristics are also shown as the discrepancies in the v-component winds in B-1 (cf. Fig. 15). The discrepancies in the u- and v-component winds in C-3 are 15 m s^{-1} and 4 m s^{-1} , respectively, in the layers between 700 m MSL and 900 m MSL . Alternative positive and negative discrepancies in the range of $-3 \text{ to } 3 \text{ m s}^{-1}$ for the u-component winds in C-3 were found above 1000 m MSL .



664
 665 Figure 16. The same as Fig.12, but (a) and (b) for C-1. (c) and (d) are the same as (a) and (b) but for C-2. (e) and (f)
 666 are the same as (a) and (b) but for C-3.



667

668 Figure 17. The same as Fig. 13 but for C-1~C-3.

669 6. Conclusion

670 A modified WISSDOM synthesis scheme was developed to derive high-quality 3D winds
 671 under clear-air conditions. The main difference from the original version is that multiple lidar
 672 observations were used, and high-resolution 3D winds (50 m horizontally and vertically) were
 673 first derived in the newly developed WISSDOM scheme. In addition, all available datasets were
 674 included as one of the constraints in the cost function in this study. The data implementation and
 675 the detailed principles of the newly developed WISSDOM were also elaborated. This newly



676 developed WISSDOM scheme was performed over the TMR to retrieve 3D winds during a strong
 677 wind event during ICE-POP 2018. The performance was evaluated via a series of sensitivity tests
 678 and compared with conventional observations.

679 The intercomparisons of horizontal winds during the entire research period reveal a relatively
 680 high correlation coefficient between the WISSDOM synthesis and sounding's u- (v-) component
 681 winds exceeding 0.97 (0.87) at the DGW site. Furthermore, the average bias is -0.78 m s^{-1} (0.09
 682 m s^{-1}), and the RMSD is 1.72 m s^{-1} (1.65 m s^{-1}) for the u- (v-) component winds. The
 683 intercomparisons of 3D winds between the WISSDOM synthesis and lidar QVP also showed a
 684 higher correlation coefficient (0.84) for u-component winds, but a relatively smaller correlation
 685 coefficient remained at 0.35 for v-component winds in this strong wind event. The average bias
 686 (RMSD) of u-component winds is 2.83 m s^{-1} (3.69 m s^{-1}), and the average bias and RMSD of v-
 687 component winds are 2.26 m s^{-1} and 2.92 m s^{-1} , respectively (cf. Table 2). Chen (2019) analyzed
 688 the correlations between 3D winds derived from radar and observations in several typhoon cases;
 689 the mean correlation coefficient ranged from 0.56 to 0.86, and the RMSD was between 1.13 and
 690 1.74 m s^{-1} . Compared to their results, only u-component winds have relatively higher correlation
 691 coefficients, but the RMSD values are slightly higher in this study, which may have been caused
 692 by the high variability in westerly winds associated with the moving LPS. The statistical error
 693 results of the winds between the WISSDOM synthesis and observations show a good
 694 performance of the retrieved 3D winds in this strong wind event (Table 3). Generally, the median
 695 values of wind directions are within 5 degrees. Compared with lidar QVP (sounding
 696 observations) the median values of the wind speed are approximately $-1\sim 3 \text{ m s}^{-1}$ ($-1\sim 0.5 \text{ m s}^{-1}$)
 697 and the vertical velocity is within $-0.2\sim 0.6 \text{ m s}^{-1}$. Compared with lidar QVP (sounding
 698 observations) above the DGW site, the interquartile range of wind directions is $-10\sim 5$ ($0\sim 2.5$)
 699 degrees, the wind speed is approximately $-4\sim 4 \text{ m s}^{-1}$ ($-3\sim 1 \text{ m s}^{-1}$) and the vertical velocity is
 700 $-0.8\sim 0.8 \text{ m s}^{-1}$.

701 A control run (see the basic setting in Table 1) was set to explore the importance of acquired



702 observation datasets, various distances of RI, VE from the AWS observations, and the weighting
 703 coefficient for each constraint (i.e., Experiments A-C, Table 4). The results of Experiment A
 704 show that the lidar and AWS play critical roles in the derived horizontal winds, and the lidars
 705 (AWSs) provided positive (negative) contributions in stronger (weaker) wind speeds near the
 706 surface. The sounding and the LDAPS provided relatively smaller impacts on the derived
 707 horizontal winds from the WISSDOM synthesis. In Experiment B, the smallest discrepancies in
 708 3D winds were depicted when the RI (VE) was set to 1 km (50%). However, there were larger
 709 discrepancies in 3D winds (from -0.4 m s^{-1} to $\sim 1 \text{ m s}^{-1}$) when the RI was set at 0.5 km and 2 km,
 710 and the VE was set between 50% and 90% (cf. Fig. 15). In Experiment C, significant
 711 discrepancies in 3D winds appeared by decreasing (raising) the weighting coefficient from the
 712 AWS observations (LDPAS datasets).

713 This study demonstrated that reasonable patterns of 3D winds were derived by the newly
 714 developed WISSDOM synthesis scheme in a strong wind event. In the future, many cases are
 715 required to check the performance of this newly developed WISSDOM scheme with different
 716 synoptic weather systems under clear-air conditions in different seasons. In addition, knowing
 717 the detailed kinematic fields will help us to identify where the flow accelerates/decelerates over
 718 complex terrain. Thus, the possible mechanisms of extremely strong winds in South Korea will
 719 be well documented through combinations with derived dynamic fields (Tsai et al., 2018, 2022),
 720 thermodynamic fields (Liou et al., 2019), observations and simulations. Furthermore, the new
 721 version of WISSDOM has broad applications in site surveys of wind turbines, wind energy,
 722 monitoring wildfires, outdoor sports in mountain ranges and aviation security.



723 *Code and data availability.* The scanning Doppler lidars, AWS, sounding and wind profiler
724 data used in this study are available through zenodo: <https://doi.org/10.5281/zenodo.6537508>.
725 The LDAPS dataset is freely available from the KMA website (<https://data.kma.go.kr>).
726
727 *Acknowledgments.* This work was supported by the National Research Foundation of Korea (NRF)
728 grant funded by the Korea government (MSIT) (No. 2021R1A4A1032646) and by the Korea
729 Meteorological Administration Research and Development Program under Grant KMI2022-
730 00310.
731
732 *Author contributions.* This work was made possible by contribution from all authors.
733 Conceptualization, CLT, GWL; methodology, CLT, YCL, and KK; software, CLT, YCL, and
734 KK; validation, KK, YCL, and GWL; formal analysis, CLT, and KK; investigation, CLT, and
735 GWL; writing—original draft preparation, CLT; writing—review and editing, GWL, YCL and
736 KK; visualization, CLT; supervision, GWL; funding acquisition, GWL. All authors have read
737 and agreed to the published version of the manuscript.
738
739 *Competing interests.* The authors declare that they have no conflict of interest.
740
741 *Special issue statement.* This article is part of the special issue “Winter weather research in
742 complex terrain during ICE-POP 2018 (International Collaborative Experiments for
743 Pyeongchang 2018 Olympic and Paralympic winter games) (ACP/AMT/GMD inter-journal SI)”.
744 It is not associated with a conference.
745
746



747 **References**

748

749 Bell, M. M., Montgomery, M. T., and Emanuel, K. A.: Air–sea enthalpy and momentum
 750 exchange at major hurricane wind speeds observed during CBLAST, *J. Atmos. Sci.*, **69**,
 751 3197–3222, <https://doi.org/10.1175/JAS-D-11-0276.1>, 2012.

752 Bell, T. M., Klein, P., Wildmann, N., and Menke, R.: Analysis of flow in complex terrain using
 753 multi-Doppler lidar retrievals, *Atmos. Meas. Tech.*, **13**, 1357–1371,
 754 <https://doi.org/10.5194/amt-13-1357-2020>, 2020.

755 Chen, Y.-A.: Verification of multiple-Doppler-radar derived vertical velocity using profiler data
 756 and high resolution examination over complex terrain, M.S. thesis, National Central
 757 University, 91 pp., 2019.

758 Choi, D., Hwang, Y., Lee, YH.: Observing Sensitivity Experiment Based on Convective Scale
 759 Model for Upper-air Observation Data on GISANG 1 (KMA Research Vessel) in Summer
 760 2018. *Atmosphere*, **30**, 17–30, 2020 (Korean with English abstract).

761 Cha, T.-Y. and Bell, M. M.: Comparison of single-Doppler and multiple-Doppler wind retrievals
 762 in Hurricane Matthew (2016), *Atmos. Meas. Tech.*, **14**, 3523–3539,
 763 <https://doi.org/10.5194/amt-14-3523-2021>, 2021.

764 Choukulkar, A., Brewer, W. A., Sandberg, S. P., Weickmann, A., Bonin, T. A., Hardesty, R. M.,
 765 Lundquist, J. K., Delgado, R., Iungo, G. V., Ashton, R., Debnath, M., Bianco, L., Wilczak,
 766 J. M., Oncley, S., and Wolfe, D.: Evaluation of single and multiple Doppler lidar
 767 techniques to measure complex flow during the XPIA field campaign, *Atmos. Meas. Tech.*,
 768 **10**, 247–264, <https://doi.org/10.5194/amt-10-247-2017>, 2017.

769 Colle, B. A., and Mass, C. F.: High-Resolution Observations and Numerical Simulations of
 770 Easterly Gap Flow through the Strait of Juan de Fuca on 9–10 December 1995. *Mon. Wea.*
 771 *Rev.*, **128**, 2398–2422,

772 Cressman, G. P.: An operational objective analysis system. *Mon. Wea. Rev.*, **87**, 367–374, 1959.



- 773 Hill, M., R. Calhoun, H. J. S. F., Wieser, A., Dornbrack, A., Weissmann, M., Mayr, G., and
 774 Newsom, R.: Coplanar Doppler lidar retrieval of rotors from T-REX, *J. Atmos. Sci.*, **67**,
 775 713–729, 2010.
- 776 Jou, B. J.-D., Lee, W.-C., Liu, S.-P., and Kao, Y.-C.: Generalized VTD retrieval of atmospheric
 777 vortex kinematic structure. Part I: Formulation and error analysis, *Mon. Weather Rev.*,
 778 **136**, 995–1012, <https://doi.org/10.1175/2007MWR2116.1>, 2008.
- 779 Kim D.-J., Kang G., Kim D.-Y., Kim J.-J.: Characteristics of LDAPS-Predicted Surface Wind
 780 Speed and Temperature at Automated Weather Stations with Different Surrounding Land
 781 Cover and Topography in Korea. *Atmosphere*, **11**, 1224.
 782 <https://doi.org/10.3390/atmos11111224>, 2020.
- 783 Kim, J.-H., R. D. Sharman, R. D., Benjamin, S., Brown, J., Park, S.-H. and Klemp, J.:
 784 Improvement of Mountain Wave Turbulence Forecast in the NOAA’s Rapid Refresh
 785 (RAP) Model with Hybrid Vertical Coordinate System, *Weather Forecast*, **34(6)**, 773–
 786 780, <https://doi.org/10.1175/WAF-D-18-0187.1>, 2019
- 787 Lee, J., Seo, J., Baik, J., Park, S., and Han, B.: A Numerical Study of Windstorms in the Lee of
 788 the Taebaek Mountains, South Korea: Characteristics and Generation
 789 Mechanisms. *Atmosphere*, **11**, 431. <https://doi.org/10.3390/atmos11040431>, 2020.
- 790 Lee, J.- T., Ko, K.- Y., Lee, D.- I., You, C.- H., and Liou, Y.- C.: Enhancement of orographic
 791 precipitation in Jeju Island during the passage of Typhoon Khanun (2012), *Atmos. Res.*,
 792 **201**, 1245–1254. <https://doi.org/10.1016/j.atmosres.2017.10.013>, 2017.
- 793 Lee, W.-C., Marks, F. D., and Carbone, R. E.: Velocity track display – A technique to extract
 794 real-time tropical cyclone circulations using a single airborne Doppler radar, *J. Atmos.*
 795 *Ocean. Tech.*, **11**, 337–356, [https://doi.org/10.1175/1520-](https://doi.org/10.1175/1520-0426(1994)011<0337:VTDTTE>2.0.CO;2)
 796 [0426\(1994\)011<0337:VTDTTE>2.0.CO;2](https://doi.org/10.1175/1520-0426(1994)011<0337:VTDTTE>2.0.CO;2), 1994
- 797 Lee, W.-C., Jou, B. J.-D., Chang, P.-L., and Deng, S.- M.: Tropical cyclone kinematic structure
 798 derived from single-Doppler radar observations. Part I: Interpretation of Doppler velocity



- 799 patterns and the GBVTD technique, *Mon. Weather Rev.*, **127**, 2419–2439,
 800 [https://doi.org/10.1175/1520-0493\(1999\)127<2419:TCKSRF>2.0.CO;2](https://doi.org/10.1175/1520-0493(1999)127<2419:TCKSRF>2.0.CO;2), 1999.
- 801 Liou, Y.-C., Wang, T.-C. C., Lee, W.-C., and Chang, Y.-J.: The retrieval of asymmetric tropical
 802 cyclone structures using Doppler radar simulations and observations with the extended
 803 GBVTD technique, *Mon. Weather Rev.*, **134**, 1140–1160,
 804 <https://doi.org/10.1175/MWR3107.1>, 2006.
- 805 Liou, Y., and Chang, Y.: A Variational Multiple–Doppler Radar Three-Dimensional Wind
 806 Synthesis Method and Its Impacts on Thermodynamic Retrieval. *Mon. Wea. Rev.*, **137**,
 807 3992–4010, <https://doi.org/10.1175/2009MWR2980.1>, 2009.
- 808 Liou, Y., Chang, S., and Sun, J.: An Application of the Immersed Boundary Method for
 809 Recovering the Three-Dimensional Wind Fields over Complex Terrain Using Multiple-
 810 Doppler Radar Data. *Mon. Wea. Rev.*, **140**, 1603–1619, [https://doi.org/10.1175/MWR-D-](https://doi.org/10.1175/MWR-D-11-00151.1)
 811 [11-00151.1](https://doi.org/10.1175/MWR-D-11-00151.1), 2012.
- 812 Liou, Y., Chen Wang, T., Tsai, Y., Tang, Y., Lin, P., and Lee, Y.: Structure of precipitating systems
 813 over Taiwan’s complex terrain during Typhoon Morakot (2009) as revealed by weather
 814 radar and rain gauge observations, *J. Hydrology*, **506**, 14–25.
 815 <https://doi.org/10.1016/j.jhydrol.2012.09.004>, 2013.
- 816 Liou, Y., Chiou, J., Chen, W., and Yu, H.: Improving the Model Convective Storm Quantitative
 817 Precipitation Nowcasting by Assimilating State Variables Retrieved from Multiple-
 818 Doppler Radar Observations. *Mon. Wea. Rev.*, **142**, 4017–4035,
 819 <https://doi.org/10.1175/MWR-D-13-00315.1>, 2014.
- 820 Liou, Y., Chen Wang, T., and Huang, P.: The Inland Eyewall Reintensification of Typhoon
 821 Fanapi (2010) Documented from an Observational Perspective Using Multiple-Doppler
 822 Radar and Surface Measurements. *Mon. Wea. Rev.*, **144**, 241–261,
 823 <https://doi.org/10.1175/MWR-D-15-0136.1>, 2016.
- 824 Mass, C. F., and Ovens, D.: The Northern California Wildfires of 8–9 October 2017: The Role



- 825 of a Major Downslope Wind Event. *Bull. Amer. Meteor. Soc.*, **100**, 235–256,
 826 <https://doi.org/10.1175/BAMS-D-18-0037.1>, 2019.
- 827 Mohr, C. G., and Miller, L. J. : CEDRIC—A software package for Cartesian Space Editing,
 828 Synthesis, and Display of Radar Fields under Interactive Control. Preprints, *21st Conf. on*
 829 *Radar Meteorology*, Edmonton, AB, Canada, Amer. Meteor. Soc., 569–574, 1983.
- 830 Oue, M., Kollias, P., Shapiro, A., Tatarevic, A., and Matsui, T.: Investigation of observational
 831 error sources in multi-Doppler-radar three-dimensional variational vertical air motion
 832 retrievals, *Atmos. Meas. Tech.*, **12**, 1999–2018, [https://doi.org/10.5194/amt-12-1999-](https://doi.org/10.5194/amt-12-1999-2019)
 833 2019, 2019.
- 834 Park, J.-R., Kim, J.-H., Shin, Y., Kim, S.-H., Chun, H.-Y., Jang, W., Tsai, C.-L. and Lee, G.: A
 835 numerical simulation of a strong windstorm event in the Taebaek Mountain Region in
 836 Korea during the ICE-POP 2018, *Atmos. Res.*, **272**, 106158,
 837 <https://doi.org/10.1016/j.atmosres.2022.106158>.
- 838 Päschke, E., Leinweber, R., and Lehmann, V.: An assessment of the performance of a 1.5 μm
 839 Doppler lidar for operational vertical wind profiling based on a 1-year trial, *Atmos. Meas.*
 840 *Tech.*, **8**, 2251–2266, <https://doi.org/10.5194/amt-8-2251-2015>, 2015.
- 841 Reed, T. R.: GAP WINDS OF THE STRAIT OF JUAN DE FUCA. *Mon. Wea. Rev.*, **59**, 373–
 842 376, [https://doi.org/10.1175/15200493\(1931\)59<373:GWOTSO>2.0.CO;2](https://doi.org/10.1175/15200493(1931)59<373:GWOTSO>2.0.CO;2), 1931.
- 843 Ryzhkov, A., Zhang, P., Reeves, H., Kumjian, M., Tschallener, T., Trömel, S., and Simmer,
 844 C.: Quasi-Vertical Profiles—A New Way to Look at Polarimetric Radar Data. *J. Atmos.*
 845 *Oceanic Technol.*, **33**, 551–562, <https://doi.org/10.1175/JTECH-D-15-0020.1>, 2016.
- 846 Tsai, C., Kim, K., Liou, Y., Lee, G., and Yu, C.: Impacts of Topography on Airflow and
 847 Precipitation in the Pyeongchang Area Seen from Multiple-Doppler Radar
 848 Observations. *Mon. Wea. Rev.*, **146**, 3401–3424, [https://doi.org/10.1175/MWR-D-17-](https://doi.org/10.1175/MWR-D-17-0394.1)
 849 0394.1, 2018.
- 850 Tsai, C.-L., Kim, K., Liou, Y.-C., Kim, J.-H., Lee, Y., and Lee, G.: Orographic-induced strong



- 851 wind associated with a low-pressure system under clear-air condition during ICE-POP
 852 2018, *J. Geophys. Res. Atmos.*, **127**, e2021JD036418.
 853 <https://doi.org/10.1029/2021JD036418>, 2022.
- 854 Tseng, Y., and Ferziger, J.: A ghost-cell immersed boundary method for flow in complex
 855 geometry. *J. Comput. Phys.*, **192**, 593–623, <https://doi.org/10.1016/j.jcp.2003.07.024>.
 856 2003.
- 857 Yu, C., and Tsai, C.-L.: Surface Pressure Features of Landfalling Typhoon Rainbands and Their
 858 Possible Causes. *J. Atmos. Sci.*, **67**, 2893–2911,
 859 <https://doi.org/10.1175/2010JAS3312.1>, 2010.
- 860 Yu, C.-K., & Tsai, C.-L. : Structural and surface features of arc-shaped radar echoes along an
 861 outer tropical cyclone rainband. *J. Atmos. Sci.*, **70**, 56– 72. [https://doi.org/10.1175/JAS-](https://doi.org/10.1175/JAS-D-12-090.1)
 862 [D-12-090.1](https://doi.org/10.1175/JAS-D-12-090.1), 2013.
- 863 Yu, C.-K., and Tsai, C.-L.: Structural changes of an outer tropical cyclone rain band encountering
 864 the topography of northern Taiwan. *Q. J. R. Meteorol. Soc.*, **143**, 1107–1122.
 865 <https://doi.org/10.1002/qj.2994>, 2017.
- 866 Yu, C.-K., Cheng, L.-W., Wu, C.-C., and Tsai, C.-L.: Outer Tropical Cyclone Rainbands
 867 Associated with Typhoon Matmo (2014). *Mon. Wea. Rev.*, **148**, 2935–2952,
 868 <https://doi.org/10.1175/MWR-D-20-0054.1>, 2020.